




Spectroscopic studies for the changes of a Cr(II) compound in solution triggered by the deprotonation of an aqua ligand

Manjuri K. Koley, Amrita Chatterjee, Anjan Chattopadhyay, Periakaruppan T. Manoharan & Aditya P. Koley

To cite this article: Manjuri K. Koley, Amrita Chatterjee, Anjan Chattopadhyay, Periakaruppan T. Manoharan & Aditya P. Koley (2015) Spectroscopic studies for the changes of a Cr(II) compound in solution triggered by the deprotonation of an aqua ligand, Journal of Coordination Chemistry, 68:12, 2065-2095, DOI: [10.1080/00958972.2015.1033412](https://doi.org/10.1080/00958972.2015.1033412)

To link to this article: <http://dx.doi.org/10.1080/00958972.2015.1033412>

 View supplementary material 

 Accepted author version posted online: 24 Mar 2015.
Published online: 28 Apr 2015.

 Submit your article to this journal 

 Article views: 63

 View related articles 

 View Crossmark data 

Spectroscopic studies for the changes of a Cr(II) compound in solution triggered by the deprotonation of an aqua ligand

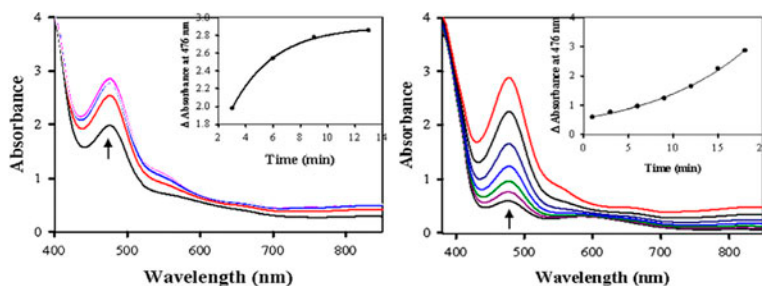
MANJURI K. KOLEY[†], AMRITA CHATTERJEE[‡], ANJAN CHATTOPADHYAY[‡],
PERIAKARUPPAN T. MANOHARAN*[§] and ADITYA P. KOLEY*[‡]

[†]Department of Chemical Engineering, Birla Institute of Technology and Science-Pilani, Zuarinagar, Goa, India

[‡]Department of Chemistry, Birla Institute of Technology and Science-Pilani, Zuarinagar, Goa, India

[§]Department of Chemistry, Indian Institute of Technology-Madras, Chennai, India

(Received 21 October 2014; accepted 11 March 2015)



Deprotonation of the aqua ligand in $[\text{Cr}(\text{OH}_2)(\text{L}^{\text{ISO}})_2]$ (**1**) is found to be essential for its dioxygen binding and activation or to undergo anaerobic change in solution. In either case the final species is found to contain reduced $-\text{NH}_2$ ligand owing to spontaneous electron transfer followed by proton addition to the oxidized $-\text{NH}$ moiety that was initially present in **1**.

Recently, we reported dioxygen binding and its activation by the Cr(II) compound $[\text{Cr}(\text{H}_2\text{O})(\text{L}^{\text{ISO}})_2]$ (**1**) [$(\text{L}^{\text{ISO}})^{1-}$ is *o*-iminothionebenzosemiquinonate(1⁻) π -radical]. In this work, we report the existence of ferromagnetism in its solid form. The plot of $(\chi_m)^{-1}$ versus T from 250 to 20 K reveals a Curie–Weiss constant of $\theta \sim 26$ K suggesting a ferromagnetic coupling. A theoretical simulation on the susceptibility curve and the fitting of the χ_m versus T yielded $g = 1.83 \pm 0.002$, $J = 33.4 \pm 0.001$ cm⁻¹, and $\theta = 25.2 \pm 0.02$ K with $J \gg D$. Increase in EPR line width on cooling helped us calculate the Cr(II)–Cr(II) distance in the proposed dimer. Also we find that deprotonation of the aqua ligand in **1** is essential for dioxygen binding and its activation. Reaction with dioxygen is completely inhibited when there is no deprotonation. Reaction of **1** with dioxygen in pyridine (py) resulted in isolation of the O=Cr(IV) compound $[\text{O}=\text{Cr}(\text{L}^{\text{AP}})_2(\text{py})]$ (**2**) [$(\text{L}^{\text{AP}})^{1-}$ is *o*-aminothiophenolate anion] and no monomeric O=Cr(V) has been detected by EPR. ¹H NMR study of **1** in *d*₆-DMSO with time shows increase in intensity of the $-\text{NH}_2$ peak at 5.46 ppm, suggesting gradual reduction of the $-\text{NH}$ groups in $(\text{L}^{\text{ISO}})^{1-}$ ligands.

Keywords: Ferromagnetically coupled Cr(II) complex; Proton NMR; EPR and electronic spectra; Oxo transfer; Electron transfer and proton transfer

*Corresponding authors. Email: ptm@iitm.ac.in (P.T. Manoharan); koleyap@yahoo.co.in (A.P. Koley)

1. Introduction

Earlier studies on the interaction of O₂ with Cr(II) compounds reveal that either it produces superoxo-Cr(III) or oxo-Cr(IV) species with different stabilities depending on the reaction conditions, solvents, and the ligand environment around Cr(II) [1–9]. Recently, we reported [10] the dioxygen binding and its activation by [Cr(H₂O)(L^{ISQ})₂] (**1**). We have now discovered that unless this compound [Cr(H₂O)(L^{ISQ})₂] undergoes deprotonation in solution to produce the [Cr(OH)(L^{ISQ})₂][−] (**B**) species, there is no dioxygen binding and its activation or there is no spectral change in the absence of air. This is intriguing because active sites containing water-coordinated metal complexes play a crucial role in the catalytic centers of many natural systems where electron transfer reactions involving the metal center are coupled to proton transfer [11]. Deprotonation of **1** in DMF was experimentally suggested from conductance and pH measurements [10], and the formation of this deprotonated species **B**, which shows a strong charge transfer band at 476 nm, was strongly favored in the presence of [N(*n*-Bu)₄]PF₆ and KSCN as well as the dioxygen binding to this deprotonated species. Similar result is obtained in the presence of sodium oxalate. However, the deprotonation of **1** in DMF is inhibited completely in the presence of oxalic acid as evident from the absence of any peak at 476 nm in the electronic spectral result (*vide infra*) and no other significant spectral change is observed with time. This clearly suggests that deprotonation of **1** in solution is crucial to bind to dioxygen or to undergo further change.

To elucidate the magnetic behavior, temperature-dependent magnetic studies were performed on **1** from 20 to 300 K. We have also performed proton NMR studies with time for **1** in d₆-DMSO to monitor its conversion to final species containing the reduced –NH₂ ligand. Also electronic spectral studies for **1** in pyridine in the presence of air, and in DMF and DMSO solutions in the absence and presence of air have been performed with time to get better understanding of the stability of the deprotonated species **B** in the absence of air and its reactivity in the presence of air. Attempt has been made based on theoretical studies to understand the mechanism involved and the nature of species generated during spontaneous spectral change of **1** in DMF in the absence of dioxygen.

2. Experimental

2.1. General remarks

Cr compounds are carcinogenic. Necessary precautions must be taken to avoid skin contact and inhalation of their solutions and dust.

2.2. Materials

o-Aminothiophenol, triphenylphosphine, triphenylphosphine oxide, tetrabutylammonium hexafluorophosphate ([N(*n*-Bu)₄]PF₆), and d₆-DMSO were obtained from Aldrich. Cr(NO₃)₃·9H₂O was obtained from Merck. Absolute ethanol (GR), methanol (GR), pyridine (GR), N,N-dimethyl formamide (DMF) (GR), and acetonitrile (HPLC) were also obtained from Merck. All other chemicals were of reagent grade and were used as obtained.

2.3. Synthesis of $[Cr(H_2O)(L^{ISO})_2]$ (1)

This compound was synthesized and characterized as reported earlier [10].

2.4. Synthesis of $[O=Cr(L^{AP})_2(py)]$ (2)

A sample of 25 mg of **1** was dissolved in ~50 mL of pyridine (py) in a stoppered conical flask in the presence of air and this solution was slowly stirred using a magnetic stirrer for 47 h at RT and filtered through a G4 sintered glass crucible. The filtrate was evaporated in vacuum to a small volume (~2 mL) and this was treated with 25 mL of CH_3CN and filtered. The CH_3CN soluble part was then concentrated in vacuum to get a dark compound. Yield: 12 mg. Anal. Calcd for $C_{17}H_{17}N_3S_2O_2Cr$ (%): C, 51.63; H, 4.34; N, 10.63. Found (%): C, 52.01; H, 4.40; N, 10.93. IR (KBr pellet, cm^{-1}): 3352br, $\nu_{as}(N-H_2)$; 3200br, $\nu_s(N-H_2)$; 1616s, $\delta(N-H_2)$; 920 m, $\nu(Cr=O)$; 536 m, br $\nu(Cr-N)$.

When a portion of the above-mentioned CH_3CN soluble part was collected in a 25-mL conical flask and kept at RT in air for slow evaporation, a dark compound was obtained after several days. This compound (**2a**) was found to be different from **2** mentioned above.

2.5. Synthesis of $[Cr(L^{AP})_2(py)]_2(\mu-OH)(OH)$ (3)

Fifty milligrams of **1** was dissolved in 75 mL of pyridine (py) in a stoppered conical flask in the presence of air and stirred at room temperature for 96 h. This solution was then filtered through a G-4 sintered glass crucible, and the solvent was evaporated in vacuum to complete dryness. To this dry mass, 15 mL of CH_3CN was added, stirred, and the dark residue (**2a**) was filtered, washed with CH_3CN , and dried. The pink CH_3CN solution was collected separately and used later for recording the electronic spectrum and then reacted with PPh_3 . The residue (**2a**) obtained after washing with CH_3CN was then dissolved in a minimum volume of DMF, filtered, and the solution was left for crystallization under vacuum for several weeks while a dark compound was obtained. This was collected by filtration, and washed with CH_3CN , and dried. Yield: 20 mg. Anal. Calcd for $C_{34}H_{36}N_6S_4O_2Cr_2$ (%): C, 51.50; H, 4.58; N, 10.60. Found (%): C, 51.71; H, 4.52; N, 10.92. IR (KBr pellet, cm^{-1}): 3448 br $\nu(O-H)$; 3345br, $\nu_{as}(NH_2)$; 3200br, $\nu_s(NH_2)$; 1605s, $\delta(NH_2)$; 1305s, $\nu(C-NH_2)$; 530 m, br $\nu(Cr-O)$ and $\nu(Cr-N)$.

2.6. Physical measurements

Elemental analyses (for C, H, and N) were performed on a Perkin-Elmer model 2400 series II CHNS analyzer. Infrared spectra were measured with Jasco IR report-100 and Shimadzu IR Affinity - 1 FT-IR spectrometers using KBr pellets. Static susceptibility measurements were made with the help of a Lakeshore VSM 7410 Vibrating Sample Magnetometer. Electronic spectra were recorded with a Jasco V-570 UV/VIS/NIR spectrophotometer using a pair of matched quartz cells of path length of 1 cm. EPR spectra were recorded using a Varian E-112 X/Q-band spectrometer. Instrumental parameters: modulation frequency = 100 kHz, modulation amplitude = 1 G, microwave power = 20 mW. Solution EPR spectra at RT were recorded using an aqueous cell. Diphenylpicrylhydrazyl (DPPH) was used as an internal field marker. Proton NMR spectra were recorded using a Bruker AVANCE III 500 MHz (AV 500) multi nuclei solution NMR spectrometer. Conductivity

measurement was done using a Mettler Toledo dual conductivity/pH meter model SevenMulti equipped with Inlab 730 and Inlab 413 electrodes. Electrochemical measurements were done with the help of a Bioanalytical system CV-27 electrochemical analyzer and a BAS model X–Y recorder at 298 K under dinitrogen. A standard three electrode cell consisting of a platinum working electrode, a platinum auxiliary electrode, and a Ag/AgCl reference electrode was used. Tetrabutylammonium hexafluorophosphate ($[N(n\text{-Bu})_4]\text{PF}_6$) was used as supporting electrolyte.

2.7. Computational details

Quantum mechanical calculations have been carried out at the density functional theory (DFT) [12] and time-dependent density functional theory (TD-DFT) [13, 14] level using Gaussian 09 program [15]. Becke's [16] three parameter exchange function (B3) with Lee–Yang–Parr correlation [17] function (LYP) has been employed using LANL2DZ basis sets for the geometry optimization calculations. The excited state analysis has been performed at the Td-B3LYP/LANL2DZ level. The relevant molecular orbitals are analyzed through the visualization software Chemcraft. The UV–vis λ_{max} value corresponding to the vertical excitation energy and the oscillator strength values are reported at the ZINDO/CI [18] (using Arguslab 4.0.1) and TDDFT level of calculations.

3. Results and discussion

3.1. Magnetic moment and possible structures at room and low temperatures

We proposed in our previous report [10] that **1**, the possible structures of which are shown in scheme 1, contained an antiferromagnetically coupled Cr(II) ion with two π -radical *o*-iminothionebenzosemiquinonate(1–) ($\text{L}^{\text{ISQ}}\text{)}^{1-}$ ligands [19] and a coordinated water in solid state. To confirm this, temperature-dependent magnetic studies were performed on **1** in the temperature region of 20–300 K. The results are given for χ_{m} versus T as well as μ_{eff} versus T in figure 1. The susceptibility data were corrected for diamagnetism using Pascal's constants.

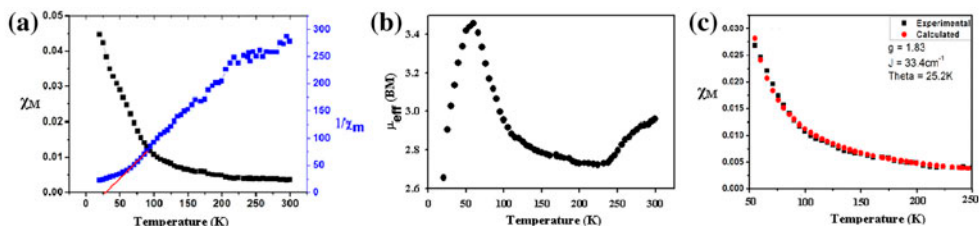
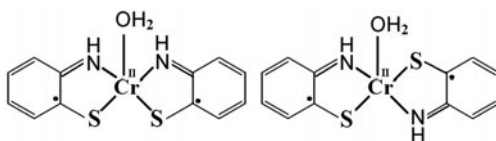
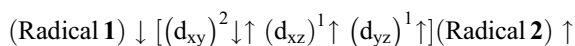


Figure 1. Variable temperature magnetic susceptibility results for **1** from 20 to 300 K. (a) Plot of diamagnetism corrected experimental susceptibility, χ_{m} vs T and its inverse $1/\chi_{\text{m}}$ vs. T from 20 to 300 K; (b) Plot of μ_{eff} vs. T , as calculated from experimental susceptibility using the spin-only formula $\mu_{\text{eff}} = 2.828(\chi_{\text{m}}T)^{1/2}$ from 20 to 300 K; (c) Fitting of experimental susceptibility using a $S_1 = S_2 = 1$ dimer model of interaction for suggested structure in figure 3 using Hamiltonian (2). Black squares (■) represent experimental and red circles (●) represent calculated values (see <http://dx.doi.org/10.1080/00958972.2015.1033412> for color version).

Scheme 1. Proposed structures of **1**.

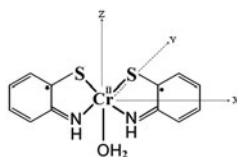
A detailed study of the compound by temperature-dependent magnetic susceptibility followed by simulation indicates the existence of paramagnetism from a two electron system with μ_{eff} value of 2.95 to 2.75 BM at 300–250 K. This suggests the presence of a Cr(II) ion in a tetragonal $\text{N}_2\text{S}_2\text{O}$ coordination from the two organic radical ligand anions and water, having an electronic configuration $d_{xy}^2 d_{xz}^1 d_{yz}^1$. It further appears that the two radical ligands interact in the manner of metal-mediated antiferromagnetism [19c, 20]; in other words, for **1** the spin arrangement can be represented by:



In giving the above arrangement of electron spins, we have taken into consideration that the metal ion is in a low-spin crystal field arrangement with C_s symmetry given the coordinate system (figure 2) for the $\text{OCr(II)N}_2\text{S}_2$.

Though both *cis*- and *trans*-structures are possible as shown in scheme 1, it was found from the optimized geometry of this compound (and also other species) that the organic N–S donor ligands are *cis* (vide infra). Hence, based on theoretical calculations, we hereafter restrict our discussion assuming a *cis* structure for **1** as shown in figure 2; here, the ligating atoms and the phenyl rings, i.e. from the free radicals, $(\text{L}^{\text{ISQ}})^{1-}$ provide their π orbitals to facilitate a strong and weak $d\pi$ – π interaction, respectively, with their electrons in the d_{xz} and d_{yz} orbitals of the Cr(II) ion of **1**. This in essence leads to the presence of two unpaired electrons in the metal ion itself and a metal-mediated antiferromagnetically coupled system in **1**, a kind of distant coupling facilitated by metal electrons which provide an exchange pathway for coupling the free radical electrons in the two L^{ISQ} units [19c].

Figure 1 (panel a) represents the experimental magnetic susceptibility corrected for diamagnetism, χ_m and inverse susceptibility $1/\chi_m$ as a function of temperature. From 250 to 300 K, the solid lattice behaves like a pure paramagnetic $S = 1$ system with $\mu_{\text{eff}} = 2.75$ – 2.95 BM in accord with the spin arrangement given above for the molecule with the proposed structure of figure 2. However, at temperatures below 250 K, if we use the simple spin-only formulation using

Figure 2. The coordinate system for the *cis* structure of **1**.

$$\mu_{\text{eff}} = 2.828(\chi_m T)^{1/2} \quad (1)$$

the μ_{eff} value shoots up to 3.5 BM (see figure 1, panel b) and falls down to a low value indicating it to be due to an exchange coupled system with the T_N being around 50 K. There is no indication of this in χ_m versus T plot given in figure 1, panel a. Furthermore, the plot of $(\chi_m)^{-1}$ versus T for the temperature region of 250–20 K reveals a Curie–Weiss constant of $\theta \sim 26$ K suggesting a ferromagnetic coupling. So a theoretical simulation was done on the susceptibility curve using a magnetic interaction Hamiltonian between two nearby Cr(II) spin systems $S_1 = S_2 = 1$,

$$H = g' \cdot \beta \cdot B \cdot S_1 + g \cdot \beta \cdot B \cdot S_2 + J S_1 \cdot S_2 + S_1 \cdot \mathbf{D} \cdot S_2 \quad (2)$$

where the first two terms are Zeeman terms for $S_1 = S_2 = 1$ of the two Cr(II) centers, the third one represents the exchange interaction between the two spin systems, and the last term is the dipolar interaction.

The simulation was done using a program from one of our laboratories [20d]. The fitting of χ_m versus T shown in figure 1(c) was extremely good with the least amount of error with $g = 1.83 \pm 0.002$, $J = 33.4 \pm 0.001 \text{ cm}^{-1}$, and $\theta = 25.2 \pm 0.02 \text{ K}$ with $J \gg D$, the calculated Curie–Weiss constant from simulation is very close to the prediction from plot of $(\chi_m)^{-1}$ versus T . We have tried fitting also with an antiferromagnetic interaction model, Bonner–Fisher model [20d], and some more, but nothing works as well as the one originating from ferromagnetic coupling between two such molecules. Following the suggested and most probable structure of the dimer as in figure 3, the origin of the ferromagnetism could be explained by (i) the overlap involving the d_{xz} – d_{xz} and d_{yz} – d_{yz} orbitals centered on two nearby Cr(II) centers and (ii) direct interaction of the $4p\pi$ – $3p\pi$ orbitals, respectively, from Cr(II) and S centers. Here, (i) and (ii) may be equal or (ii) > (i), the spin pathway being Cr(II)–S–Cr(II). This structure also proposes a longer distance for Cr(II)–Cr(II) justifying the observed ferromagnetic interaction.

Such a structure [19c] is possible in solid state to accommodate close packing in view of the sixth position being vacant in **1**. Furthermore, cooling creates compactness in the lattice, though leading to a rather long-distance interaction between two Cr(II) ions. This structure has been suggested to represent direct $d\pi$ – $d\pi$ interaction between the two d_{xz} and d_{yz} orbitals centered on the two Cr(II) ions and $p\pi$ – $p\pi$ interaction between the $p\pi$ orbitals of the

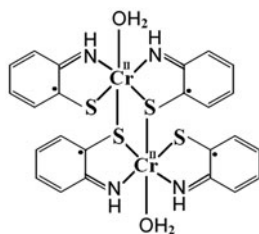


Figure 3. Proposed structure of a possible (μ -S,S)-bridged dimer using the *cis* disposition of the ligands to explain ferromagnetism.

corresponding ligands in the two constituent molecules of $[\text{Cr}(\text{H}_2\text{O})(\text{L}^{\text{ISQ}})_2]$, predicting a rather longer Cr(II)–Cr(II) bond and hence ferromagnetic coupling. Had the interionic bond Cr(II)–Cr(II) been stronger, we could have ended up with antiferromagnetic coupling. The total magnetism can be explained by the Hamiltonian (2), where $S_1 = S_2 = 1$ from the individual molecules **1** of the dimer before coupling, J represents the intermolecular exchange coupling between the two $S = 1$ systems. The first two terms in equation (2) will become a single term $g \cdot \beta \cdot B \cdot S$ for understanding the magnetic property above 250 K. Hence, the g' for the dimer will be different from the g value of the monomeric molecules. Hence, the proposed structure at low temperatures will be represented by figure 3 though at higher temperatures, the intermolecular interaction is weaker or simply absent. In this context, it is necessary to recall the change of g values and the line widths (ΔH_{pp}) of $[\text{Cr}(\text{H}_2\text{O})(\text{L}^{\text{ISQ}})_2]$ at RT and LNT [10]. The values are, respectively, 1.972 and 500 G and 2.039 and 800 G at these two temperatures, both EPR spectral lines being isotropic. The differences in g value as well as, most importantly, increased EPR line width are justified by the proposed structure in figure 3. The increase in-line width from 500 G at RT to 800 G at low temperature should be due to dimer formation and this increase can be used to calculate the Cr(II)–Cr(II) distance in the dimer. Such calculations have been earlier done by groups of workers [20e, f] to calculate interdimer distance using the following equation (3):

$$D^{\text{dip}}(\text{in } 10^{-4} \text{ cm}^{-1}) = 0.4333 g^2/r^3 \quad (3)$$

where r is the interdimer distance in Å. The increased line width of 300 G corresponds to $285.59 \times 10^{-4} \text{ cm}^{-1}$. Cr(II)–Cr(II) distance by this calculation is 3.98 Å. It is comparable to Cu(II)–Cu(II) distances of the order of 3.55–3.77 Å [20f]; this value is an indication of dimer formation. In fact, D and J values suggest the formation of dimer on cooling due to contraction of the lattice. If it is natural dimers, the distance value could have gone down further. The change in the two parameters at LNT is most likely due to a transformation from a monomeric entity to a dimer because of lattice contraction at lower temperatures, especially below 250 K, where the exchange and dipolar interactions from the compacted dimers prevail with J dominantly contributing to the experimental susceptibility and the dipolar term being very small, i.e. $D \ll J$ but contributing to increased EPR line width at LNT. The use of Hamiltonian (2) is justified by the fact $J \gg D$.

3.2. ^1H NMR results

We reported earlier [10] that **1** undergoes spontaneous change in solution, either in the absence or presence of air and it was inferred from the conductivity and pH measurements of its DMF solution at RT that the coordinated water undergoes rapid deprotonation to produce a Cr(OH) species. To confirm the generation of a Cr(OH) species in solution, we have now studied the change of this compound in DMSO at RT using UV–visible and NMR spectroscopies. The UV–visible spectroscopic change in the NIR and visible region clearly show (figure S1 [see online supplemental material at <http://dx.doi.org/10.1080/00958972.2015.1033412>]) that the compound behaves very similar as observed in its DMF solution [10] except that the change in DMSO is much slower than that observed in DMF. We have recorded the ^1H NMR spectra of this compound in d_6 -DMSO in the absence and presence of methanol, a scavenger of CrO^{2+} species, with time to study this change. The NMR spectra of the fresh solution in the absence of methanol clearly displayed a weak broad peak at

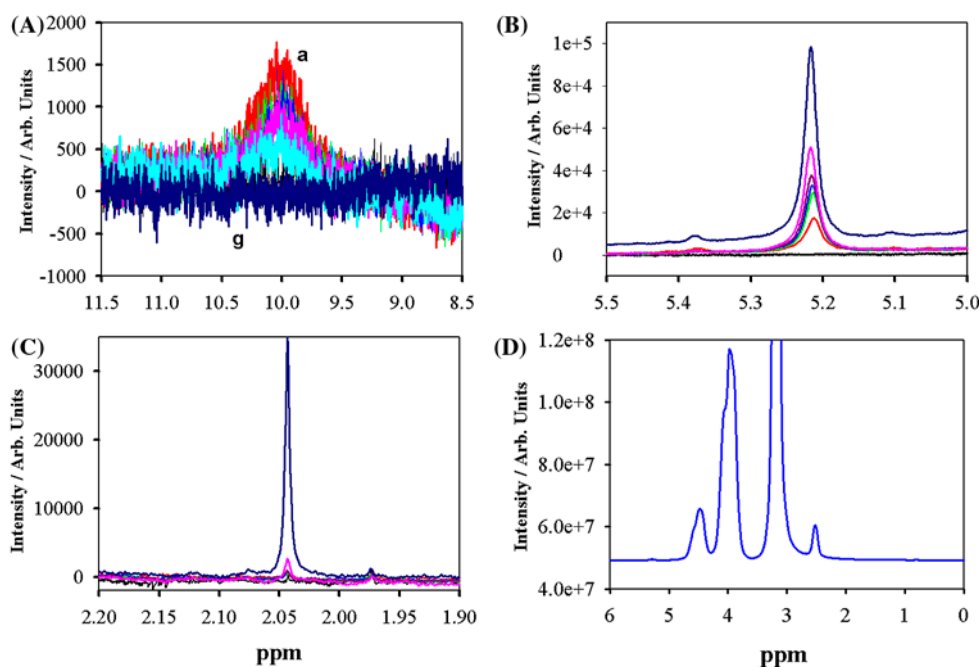


Figure 4. ¹H NMR results of **1** in d₆-DMSO (300 μL) containing methanol (200 μL). Panel A: Disappearance of OH peak with time. Top red curve *a* recorded within 15 min of making the fresh solution, cyan curve was recorded after 5 h, and the dark blue curve *g* at the bottom was recorded after 24 h. Panel B: Appearance of NH₂ signal with time. Bottom red curve was recorded within 15 min of making the fresh solution, pink curve was recorded after 5 h, and the dark blue curve on the top was recorded after 24 h. Panel C: Formation of the 2.04 ppm peak with time. Bottom red curve was recorded within 15 min of making fresh solution, pink curve was recorded after 5 h, and the dark blue curve on the top was recorded after 24 h. Panel D: After treatment with D₂O. A new peak appeared at 4.48 ppm with a shoulder at 4.6 ppm while the peak at 2.04 ppm disappeared when the final solution after 24 h mentioned above was equilibrated with D₂O for 24 h (see <http://dx.doi.org/10.1080/00958972.2015.1033412> for color version).

10.32 ppm which is shifted to 10.01 ppm in the presence of methanol [figure 4 (panel A, top red curve *a*)] and this peak slowly decreases in intensity and ultimately disappears completely after 24 h [figure 4 (panel A, bottom dark blue curve *g*)].

Thus, the appearance of this OH peak clearly suggests the presence of a coordinated –OH in the initial species present in the fresh solution and it slowly disappears with time. The gradual disappearance of this OH peak at 10.01 ppm is due to the formation of new species upon O₂ binding to the deprotonated species followed by its conversion to other products as described earlier by Koley *et al.* [10]. On the other hand, a sharp peak at 5.21 ppm (5.46 ppm in the absence of methanol) which also grows with time suggests the presence of –NH₂ protons in the final product [figure 4 (panel B)]. There is another peak appearing at 2.04 ppm and its intensity increases with time as shown in figure 4, panel C. This peak most likely arises due to coordinated water [21] in the final product generated in solution. When this solution is treated with D₂O for 24 h, this peak at 2.04 ppm disappears completely and a new peak appears at 4.48 ppm with a shoulder at 4.6 ppm [figure 4 (panel D)], possibly due to the presence of HOD. Also, the intensity of the –NH₂ signal at 5.21 ppm drastically reduced, as expected, on treatment with D₂O [figure 4 (panel D)].

Comparisons of the ^1H NMR spectra of **1** in d_6 -DMSO (300 μL) containing methanol (200 μL) recorded with time are shown in figures S2–S4 of the Supplementary Material.

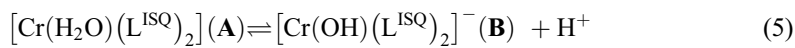
3.3. Electronic spectra

A freshly prepared DMF solution of $[\text{Cr}(\text{H}_2\text{O})(\text{L}^{\text{ISQ}})_2]$ (**1**) shows a strong charge transfer band at 476 nm (figure 5 curve *a*) that abruptly changes in the second scan (within 2 min of the first scan) in the presence of dioxygen (figure 5 curve *b*). In the absence of dioxygen, the intensity of the peak at 476 nm increases and remains steady up to 13 min in DMF (figure 6, top panel A) and then starts decaying as evident from the decrease of this peak at 476 nm (figure S5, panel B of the Supplementary Material). Data for the plot of absorbance change (increase in absorbance at $\lambda_{\text{max}} = 476$ nm) with time were fitted (figure 6, inset in top panel A) using the single exponential model

$$\Delta A_t = c + a(1 - e^{-kt}) \quad (4)$$

which resulted in the kinetic parameters: $c = 0.5 \pm 0.2$, $a = 2.4 \pm 0.1$, k (min^{-1}) = 0.32 ± 0.02 indicating a slow process.

Compound **1** undergoes spontaneous deprotonation due to the following equilibrium [10]



and the deprotonated species **B** that displays a strong charge transfer band at 476 nm readily reacts with dioxygen; this peak at 476 nm abruptly changes in the second scan (figure 5). This does not happen in the absence of air as evident from figure 6. In aerobic condition, the change of the 476 nm peak is found to be faster in DMF in the presence of sodium oxalate than in its absence [10] as evident from the rapid growth of the 548 nm peak reaching its maximum intensity and then decaying with time (figure 7, panel A). This suggests that the deprotonation is favored in the presence of sodium oxalate and the equilibrium shown in equation (5) is shifted to the right since the deprotonated species **B** readily binds to

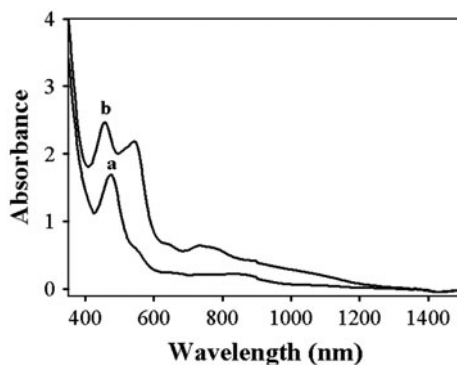


Figure 5. Electronic spectral changes of a freshly prepared DMF solution of **1** (7.20×10^{-4} mol L^{-1}) in the presence of air. (a) First scan within 2 min and (b) second scan within 5 min.

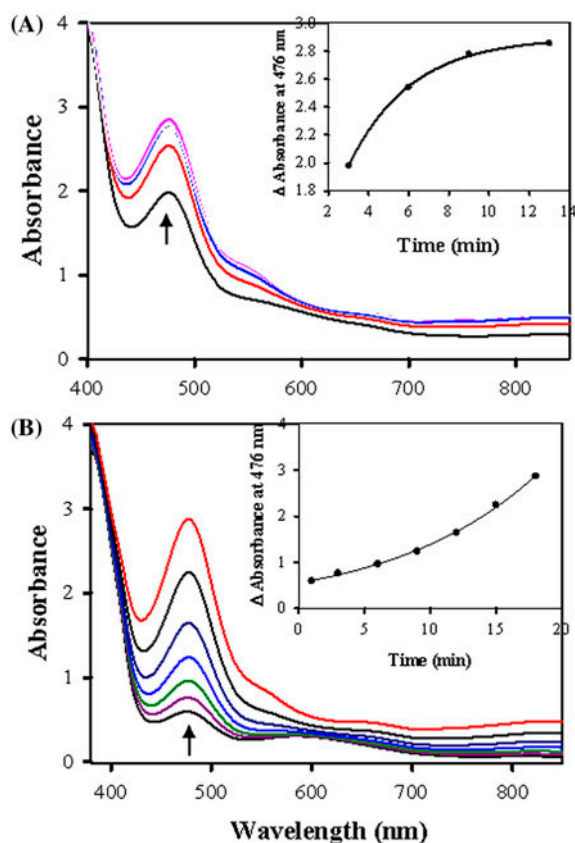


Figure 6. Electronic spectral changes of **1** in the absence of air showing the increase in intensity of the 476 nm peak reaching a maximum intensity with time before it starts decaying. Panel A shows the change of **1** in DMF ($8.12 \times 10^{-4} \text{ mol L}^{-1}$) and panel B shows the change of **1** in DMSO ($1.27 \times 10^{-3} \text{ mol L}^{-1}$), both in dinitrogen. Inset shows the plot of absorbance change at 476 nm with time in each case.

dioxygen when the 476 nm peak rapidly changed and the peak at 548 nm reached maximum intensity and then started decaying with time. However, the deprotonation of **1** in DMF is completely inhibited in the presence of oxalic acid as evident from the absence of any peak at 476 nm and only a broad peak centered around 562 nm is observed in the electronic spectrum in the presence of air with little spectral change with time as monitored for a period of 210 min (figure 7, panel B). This broad peak at 562 nm likely arises due to the protonated original compound **1** containing the aqua ligand because this peak is also observed as a broad shoulder around 562 nm along with the 476 nm peak in the first scan of the electronic spectrum of **1** in DMF in dinitrogen (figure 6, bottom black curve in panel A). This is more prominent in the electronic spectrum of **1** in DMSO in dinitrogen (figure 6, bottom curve in panel B) where this broad band is red shifted to $\sim 571 \text{ nm}$ and is clearly observed along with the peak at 476 nm in the very first scan due to slow deprotonation of **1** in DMSO as compared to that in DMF. It is highly unlikely that this contrasting spectral behavior of **1** in DMF containing oxalic acid from that containing sodium oxalate (figure 7), both in the presence of air originates from the coordination of oxalate, in that case, we should have similar results using sodium oxalate also. Thus, it is strongly indicative that the

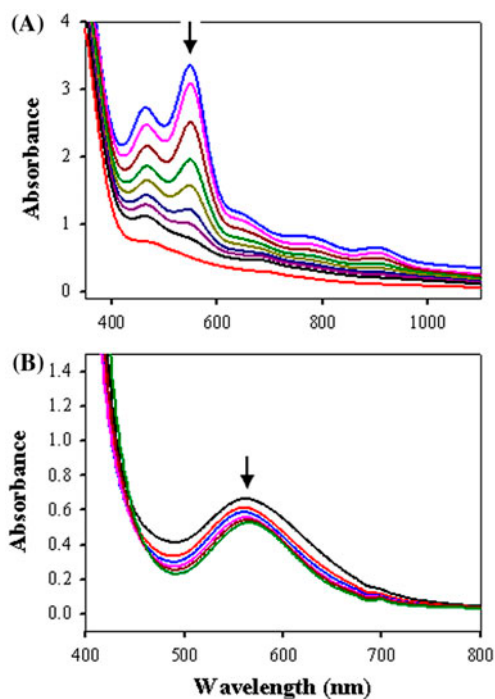


Figure 7. Panel A: Electronic spectral change of a freshly prepared DMF solution of **1** ($1.02 \times 10^{-3} \text{ mol L}^{-1}$) containing twofold excess sodium oxalate in the presence of air. The peak at 476 nm, as shown in figure 5, very rapidly changed after reacting with dioxygen producing a peak at 548 nm that reached maximum intensity within 10 min and then started decaying with time. Total time taken for the decay is 280 min. Panel B: Electronic spectral change of a freshly prepared DMF solution of **1** ($7.02 \times 10^{-4} \text{ mol L}^{-1}$) containing twofold excess oxalic acid in the presence of air. Top black curve was recorded within 2 min that changes very slowly with time (recorded up to 270 min).

difference originates due to the addition of H^+ ions from the dissociation of the oxalic acid in DMF that suppresses the deprotonation of **1** and its subsequent binding to dioxygen. So it is clear that unless there is deprotonation of **1**, it does not undergo any significant change in the absence or presence of dioxygen.

We have also studied the stability of the deprotonated species in DMF containing different alcohols (2:1 v/v) in the presence of dioxygen and noted that the peak at 476 nm did not change abruptly in the presence of any of these alcohols mentioned and the intensity of the peak at 476 nm continued increasing up to certain time depending on the alcohol, and then its position started changing slowly after reacting with dioxygen (figure 8). The reaction of the deprotonated species with dioxygen is delayed in the presence of the alcohols, thereby increasing the concentration of the deprotonated species; it is found to be maximum (20 min) for ethanol before it appreciably reacts with dioxygen as seen from the spectral changes (figure 8). The stability in the presence of these alcohols follows the order:

$$\text{ethanol} > \text{isopropanol} \sim n\text{-butanol} > \text{methanol} \sim t\text{-butanol} \quad (5)$$

and the stability in the presence of ethanol is almost double than that in the presence of methanol or *t*-butanol.

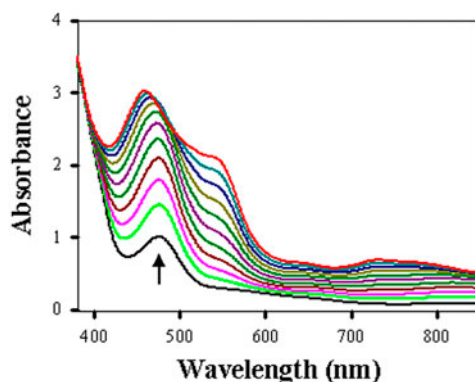


Figure 8. Electronic spectral change of **1** (9.2×10^{-4} mol L⁻¹) in DMF containing C₂H₅OH (2:1) in the presence of air at RT showing the increase in intensity of the 476 nm peak with time up to 20 min before it appreciably changes in contrast to that shown in figure 5 in the absence of C₂H₅OH where the peak at 476 nm abruptly changed in the second scan within 5 min.

3.3.1. Pyridine solution in the presence of air. The spectrum of a fresh solution of **1** in pyridine in the presence of air was recorded immediately after making the solution. This spectrum [figure 9 (curve *a* in panel A)] displays a strong band at 401 nm followed by strong absorption in the UV region and shows only weak absorption in the NIR and lower energy of the visible region. However, the spectrum slowly changes with time as evident from the second and third scans [figure 9 (curves *b*, *c* in panel A)], and the color of the solution gradually became dark within 30 min and new absorptions then start appearing at 1249, 853, 692, and 482 nm in the NIR and visible regions [figure 9 (curve *d* in panel A)]. The intensity of the bands at 1249 and 853 nm rapidly increases and reaches a maximum and becomes steady within 75 min [figure 9 (curves *g*-*i* in panel A)]. The intensity of these two bands then decreased followed by increase in intensity of a band at 692 nm [figure 9 (curves *j*-*w* in panel B)]. Finally, the intensity of the latter band at 692 nm became steady while the band at 853 nm becomes weak and the band at 1249 nm almost disappears after about 47 h [figure 9 (curve *y* in panel C)]. The second phase of this spectral change, i.e. decrease in intensity of the bands at 853 nm and 1249 nm proceeded via at least one isosbestic point at 759 nm [figure 9 (curves *j*-*w* in panel B)], indicating a direct conversion without the involvement of a third species in this phase. The plot of absorbance change with time for the appearance of the peak at 1249 with time [shown in figure 9 (panel A)] is found to be sigmoid, and the disappearance of the peak at 1249 nm [shown in figure 9 (panel B)] was exponential and fitted using the two exponential model $\Delta A_t = a_1 e^{-k_1 t} + a_2 e^{-k_2 t}$, which yielded $a_1 = 0.55 \pm 0.02$, $k_1 = 0.0061 \pm 0.0004$ min⁻¹, $a_2 = 0.92 \pm 0.02$, and $k_2 = 0.00060 \pm 0.00002$ min⁻¹, respectively. This clearly shows the involvement of two species that are associated with the very slow decay of the 1249 nm peak. These results are presented in figure S6 of the Supplementary Material.

The spectrum became steady after ~47 h [figure 9 (curve *y* in panel C)], then solid PPh₃ was added to this solution and spectrum was recorded [figure 9 (curve *z* in panel C)]. A significant change in spectrum was observed. Evaporation of this solution yielded an unknown chromium compound and O=PPh₃. This latter compound was isolated from the reaction mixture, purified from CH₂Cl₂-toluene, and characterized by comparing its IR and electronic spectra with that of an authentic sample of triphenylphosphine oxide. In the

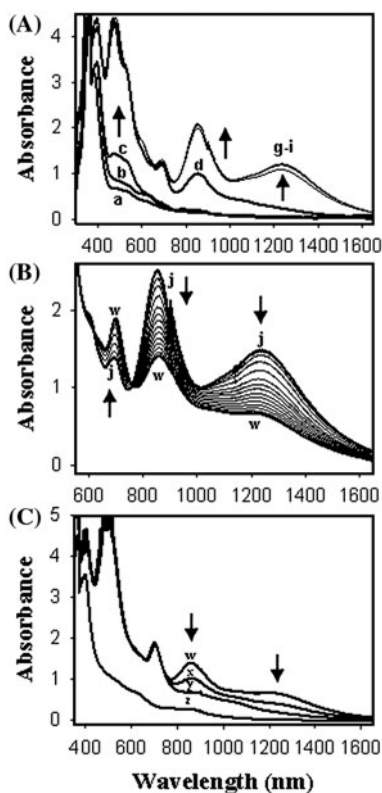
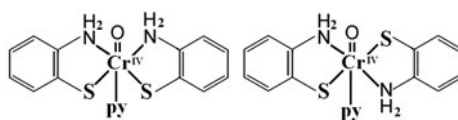


Figure 9. Electronic spectral change of **1** in pyridine. Concentration used for experiment in Panel A was $0.75 \times 10^{-3} \text{ mol L}^{-1}$ and that for Panels B and C were $0.86 \times 10^{-3} \text{ mol L}^{-1}$. Panel A shows increase in intensity at 1249, 853, and 692 nm to reach a steady state: (a) within 2 min, (b) at 12 min, (c) at 22 min, (d) at 32 min, (e) at 42 min, (g–i) 60–80 min. Panel B shows decrease in intensity at 1249 and 853 nm while increasing in intensity at 692 nm: (j) at 75 min when reached maximum intensity, (w) after 10 h. Panel C shows the spectral change at the end of the second phase for the conversion of **1** possibly to a O=Cr(IV) species and its reaction with PPh₃ in pyridine at RT: (y) after ~47 h, (z) after adding PPh₃ (at completion of its reaction with PPh₃ within 15 min).

absence of PPh₃, the absorbance change in the last phase is very slow, indicating that the decay of the O=Cr(IV) species (vide infra) that was formed in the second phase is also very slow leading to another product (**2a**) isolated from the pyridine solution after 96 h (experimental). Since the decay of the intermediate formed after 47 h was very slow, we could isolate this intermediate (**2**) from pyridine solution and characterize it (experimental). Attempt to recrystallize **2** from CH₃CN by keeping the solution at RT for several days resulted in the formation of **2a** as indicated from its electronic spectrum and its reaction



Scheme 2. Proposed structures of **2**.

with PPh_3 . However, both **2** and **2a** when dissolved in DMF and allowed to stand at RT for several days led to the isolation of **3** (*vide* scheme 3).

The IR spectrum of **2** clearly shows the presence of $\delta(\text{NH}_2)$ at $\sim 1610\text{ cm}^{-1}$ indicating the presence of the $-\text{NH}_2$ groups in aromatic ligands and another strong band at 1440 cm^{-1} indicating the presence of pyridine. Also, the intense band at 1116 cm^{-1} in the IR spectrum of **1** (supplementary figure S7) indicates the presence of $\nu(\text{C}=\text{S}^\cdot)$ and has been established as a marker for the presence of the π -radical anion [10] and is found to be absent in the IR spectra of the isolated **2** and **3**. Apart from these, a medium intensity broad band observed around 920 cm^{-1} is absent in the IR spectrum of **3**. The band at $\sim 920\text{ cm}^{-1}$ likely arises due to $\nu(\text{Cr}=\text{O})$ of this $\text{O}=\text{Cr}(\text{IV})$ species. The lowering of the $\nu(\text{Cr}=\text{O})$ may be attributed to coordination of the pyridine ligand *trans* to oxo [22]. Similar results are reported for $\text{O}=\text{Cr}(\text{V})$ salen [salen = N,N' -ethylenebis(salicylideneaminate)] complexes by Kochi and coworkers [22b, c] where pyridine N-oxide (and also other monodentate ligands) coordination *trans* to oxo causes weakening of the Cr-oxo bond that was readily apparent in the infrared spectrum by a shift of $\nu(\text{Cr}=\text{O})$ from *ca.* 1004 cm^{-1} in the five-coordinate precursor to 943 cm^{-1} in the six-coordinate adduct formed upon ligation of pyridine N-oxide. Also, there are reports of $\text{O}=\text{Cr}(\text{IV})$ complexes in which the $\nu(\text{Cr}=\text{O})$ is observed in the range of 922 and 905 cm^{-1} [3a, 4].

The electronic spectrum of **2** in CH_3CN (red-purple solution) displays a strong band (figure 10, curve *a*) at 500 nm ($\epsilon = 1249\text{ M}^{-1}\text{ cm}^{-1}$) and a medium intensity band at 705 nm ($\epsilon = 716\text{ M}^{-1}\text{ cm}^{-1}$) as observed after 47 h during the change of **1** in pyridine solution, apart from a broad band around 1000 nm ($\epsilon = 398\text{ M}^{-1}\text{ cm}^{-1}$).

Addition of solid PPh_3 (1:2) to this CH_3CN solution led to immediate disappearance of all these three bands in the visible and NIR regions (figure 10, curve *b*), as observed in case of addition of PPh_3 in pyridine solution after 47 h (figure 9, curve *z*) and the color of the solution was discharged from red-purple to pale yellow. This solution was evaporated in vacuum to dryness and then treated with dry toluene. The toluene soluble part yielded a white organic compound that was purified and characterized by IR and electronic spectra and turned out to be $\text{O}=\text{PPh}_3$. To ensure that the source of oxygen for the oxide formation is from the Cr complex, and not from air, we carried out the reaction of isolated **2** with PPh_3 in carefully degassed CH_3CN solution purged with nitrogen and evaporated the solvent in vacuum and then extracted $\text{O}=\text{PPh}_3$ using degassed toluene. No $\text{O}=\text{PPh}_3$ formation

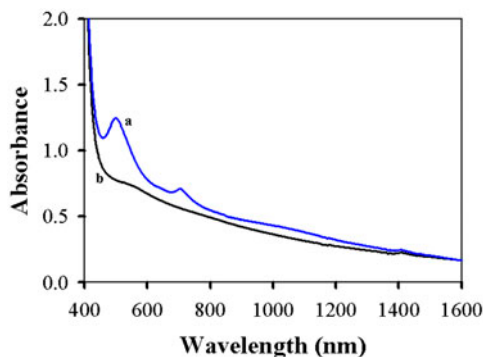


Figure 10. Electronic spectrum of (a) $[\text{O}=\text{Cr}(\text{L}^{\text{AP}})_2(\text{py})]$ (**2**) ($1.01 \times 10^{-3}\text{ mol L}^{-1}$) in CH_3CN in the presence of air; (b) after adding twofold excess of solid PPh_3 .

was observed when the same experiment was carried out in the absence of **2**. Thus, it is strongly suggestive that the intermediate Cr compound **2** is responsible for this rapid *oxo* transfer reaction, which is possible only by a O=Cr(IV) or a O=Cr(V) species under the experimental conditions. The CH₃CN solution of **2** does not exhibit any EPR signal at RT, indicating the absence of any d¹ O=Cr(V) species. It is to be recalled here that the pyridine solution also did not exhibit any d¹ Cr(V) EPR signal at RT at any stage during the conversion of **1** in pyridine at RT in the presence of air. Conductance measurement shows **2** is a nonelectrolyte in CH₃CN. Thus, it is a O=Cr(IV) compound and the *oxo* transfer is due to the following reaction



Since all three bands at 1000, 705, and 500 nm disappeared upon reaction with PPh₃, it is strongly suggestive that these three bands are associated with Cr^{IV}=O and most likely the latter two bands at 705 and 500 nm originating from Cr^{IV}=O charge transfer transitions. The resultant Cr(II) compound [Cr(L^{AP})₂(py)] displays only a weak band at ~540 nm (figure 10, curve *b*) in this region.

Based on the physicochemical properties, the proposed structure for **2** is shown in scheme 2. Though both *cis*- and *trans*-isomers are possible for **2**, optimized geometry from the theoretical calculations led to the *cis* isomer **1** (vide infra).

It appears from the solution EPR results that **2** does not undergo disproportionation to produce a Cr(III) and a O=Cr(V) species as usually observed for other O=Cr(IV) species in aqueous solution that is normally catalyzed by Mn²⁺ ions [10, 23]. This is not surprising because this is not the case always in nonaqueous solutions. For example, there is no report of such disproportionation for [Cr^{IV}=O(TPP)] (TPP = dianion of $\alpha\beta\gamma\delta$ -tetraphenylporphyrin) [7, 8] and it is highly stable in toluene or in dichloromethane. In fact, the corresponding chromium(V) porphyrinate complex, on standing, decomposed to the highly stable oxochromium(IV) complex [Cr^{IV}=O(TPP)] and this latter compound undergoes *oxo* transfer with PPh₃ in degassed dichloromethane purged with nitrogen producing O=PPh₃ [8].

A freshly prepared DMF solution of **2** displays bands at ~1000, 702, and 497 nm (figure 11, curve *a*). When reacted with twofold excess of solid and dry MnCl₂, the intensity of the bands at 702 and 497 nm increased and became steady within a few minutes with little change in the 1000 nm band but the peak at 497 nm is slightly blue shifted to 494 nm (figure 11, curve *b*). This is in contrast to those observed in the reaction of Mn²⁺ ions with other O=Cr(IV) species in nonaqueous media where the absorbance was either decreased [10] or increased [24] over a period of time to reach the steady state. These observations strongly suggest that Mn²⁺ forms a bridging complex Cr^{IV}-O-Mn^{II} which does not undergo internal electron transfer [23], resulting in Cr^{III}-OH and Mn^{III} species in the present case because the electronic spectrum (figure 11, curve *b*) clearly shows the presence of the bands at 702 and 494 nm with increased intensity while the band at 1000 nm remained unaffected after reacting with Mn²⁺, and this spectrum is typical for the presence of oxo-Cr(IV) species as observed in figure 11, curve *a* as well as in figure 10, curve *a*. Reaction of this resultant solution with solid PPh₃ led to decrease in intensity of the band at 494 nm while the bands at 702 and 1000 nm disappeared (figure 11, curve *c*) when allowed to stand overnight; addition of excess solid PPh₃ did not cause any further change in the spectrum. This indicates the formation of an oxo- or hydroxo-bridged dimeric species where Cr(IV) is reduced to Cr(III) after reacting with PPh₃ in the present case.

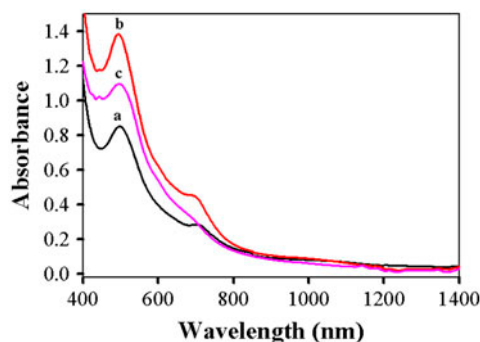


Figure 11. Electronic spectrum of (a) $[\text{O}=\text{Cr}(\text{L}^{\text{AP}})_2(\text{py})]$ (**2**) ($7.0 \times 10^{-4} \text{ mol L}^{-1}$) in DMF in the presence of air; (b) after adding twofold excess of solid Mn^{2+} , when 497 nm peak reaches maximum intensity after reacting with Mn^{2+} ; and (c) after recording curve *b*, excess solid PPh_3 was added and recorded when there was no further change in the 500 nm peak intensity.

We have also studied the change of **2** in pyridine at RT. A freshly prepared solution of **2** in pyridine in the presence of air at RT exhibited bands at ~ 1000 , 702, and 503 nm (figure 12, curve *a*). On standing, the intensity of the peak at 503 nm slowly increased with time and became steady within 48 h while the intensities of the peaks at 1000 and 702 nm remained almost unchanged (figure 12, curve *b*). Then, solid PPh_3 (1:2 ratio) was added to this solution and spectrum was recorded. There was a decrease in the intensity of the 503 nm peak but the peaks at 1000 and 702 nm disappeared (figure 12, curve *c*) in contrast to that happened in the case of a freshly prepared CH_3CN solution of **2** with PPh_3 where all these three peaks disappeared immediately and completely (figure 10, curve *b*). During the study of the electronic spectral change of **1** in pyridine, the species generated in solution after ~ 47 h when the spectrum became steady [figure 9 (curve *y* in panel C)] also displayed bands at ~ 1000 , 695, and 500 nm. All these bands completely disappeared when solid PPh_3 was added and spectrum was recorded [figure 9 (curve *z* in panel C)]. These results clearly indicate that **2** slowly forms a oxo-bridged Cr(IV)–Cr(IV) dimer on standing in pyridine

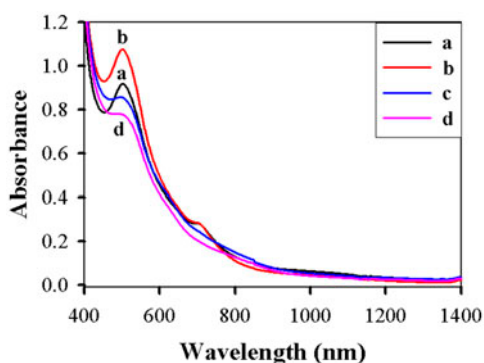


Figure 12. Electronic spectrum of (a) freshly prepared solution of $[\text{O}=\text{Cr}(\text{L}^{\text{AP}})_2(\text{py})]$ (**2**) ($7.4 \times 10^{-4} \text{ mol L}^{-1}$) in pyridine in the presence of air, (b) after allowing it to stand at RT for 48 h, (c) after recording curve *b*, twofold excess of solid PPh_3 was added, and (d) after 12 h from the time of addition of PPh_3 and recording the spectrum shown in (c).

and this dimer undergoes reduction upon reacting with PPh₃ producing an oxo- or hydroxo-bridged Cr(III)–Cr(III) compound and O=PPh₃. The formation of this latter compound has been confirmed after its isolation and purification from solution. Formation of either an oxo- or hydroxo-bridged Cr(III)–Cr(III) compound is suggested from the disappearance of the bands at 1000 and 702 nm but with the presence of the band at 503 nm (figure 12, curve *d*). It may be mentioned here in this context that Creager and Murray [25] have reported the formation of an oxo-bridged Cr(IV)–Cr(IV) dimer Cl(TPP)Cr–O–Cr(TPP)Cl in the reaction of a 2:1 mixture of [Cr(TPP)Cl] and iodosobenzene that exhibits remarkably similar electronic spectrum with that of [O=Cr(TPP)] (where TPP = meso-tetraphenylporphinate) but is distinctly different in reactivity toward olefins.

Very recently Veige and coworkers [26] have shown the marked influence of μ -oxo Cr^{IV} dimer formation ([Cr^{IV}]₂(μ -O)) and donor ligands in oxygen-atom-transfer reaction of [BuOCO]Cr^V(O)(THF) (where ^tBuOCO = [2,6-C₆H₃(6-^tBuC₆H₃O)₂]³⁻, THF = tetrahydrofuran) to PPh₃. This Cr^{IV}–O–Cr^{IV} dimer, {[^tBuOCO]Cr^{IV}(THF)}₂(μ -O), was formed during the O₂ activation by the trianionic pincer chromium(III) complex [^tBuOCO]Cr^{III}(THF)₃ to form [^tBuOCO]Cr^V(O)(THF) and was found to be in equilibrium with the reactant and the product. This compound {[^tBuOCO]Cr^{IV}(THF)}₂(μ -O) has been isolated as a solid for the first time and structurally characterized using X-ray crystallography [27].

A freshly prepared pink solution of **2a** in CH₃CN produces two weak bands at ~1000 and 700 nm and a medium intensity band at 501 nm ($\epsilon = 1366 \text{ M}^{-1} \text{ cm}^{-1}$) followed by strong charge transfer bands with a shoulder at 340 nm ($\epsilon = 7205 \text{ M}^{-1} \text{ cm}^{-1}$) in the UV region (figure 13, curve *a* of panel A). When twofold excess of solid PPh₃ was added to this pink solution and the spectrum was recorded, the intensity of the peak at 501 nm decreased with time (figure 13, curves *b–e* of panel A) and became steady on standing overnight while the shoulder at 340 nm and the weak peaks ~1000 and 700 nm disappeared completely (figure 13, curve *e* of panel A). This clearly shows that reaction of **2a** with PPh₃ in a freshly prepared CH₃CN solution is very different from that of **2** with PPh₃ in the same solvent (figure 10), clearly showing the differences in their molecular and electronic structures. As observed from its behavior in pyridine, **2** has a spontaneous tendency to form an oxo-bridged Cr(IV)–(Cr(IV) dimer; it is proposed that **2a**, which was isolated from the CH₃CN solution of **2** on prolonged standing, is also the same dimer, possibly with the formula {[Cr^{IV}(L^{AP})₂(py)]₂(μ -O)}(OH)₂ because both **2** and **2a** when dissolved in DMF and left in air for slow evaporation for crystallization led to the isolation of the powder sample {[Cr^{III}(L^{AP})₂(py)]₂(μ -OH)}(OH) (**3**) (experimental).

We have also monitored the electronic spectral change for conversion of **2** to **3** in DMF at RT. A fresh solution of **2** in DMF shows a weak but broad band around 1000 nm, a weak band at 703 nm, and a medium intensity band at 498 nm followed by another charge transfer band in the UV region with a shoulder at 350 nm (figure 13, curve *a* of panel B). The intensity of these peaks started decreasing very slowly with time and became steady only after 14 days when the weak peaks around 1000 and 703 nm disappeared completely (figure 13, curve *d* of panel B). Addition of excess PPh₃ to this solution further decreased the intensity of the 498 nm peak while the shoulder at 350 nm completely disappeared on standing overnight at RT (figure 13, curve *f* of panel B). Thus, the behavior of **2** in DMF is different from that observed in CH₃CN and pyridine where **2** spontaneously dimerized to Cr(IV)–O–Cr(IV) with the metal ions in the same oxidation states as indicated from the presence of all these bands around 1000, 703, and 498 nm, but in DMF slow reduction takes place as indicated from the disappearance of the bands around 1000 and 703 nm

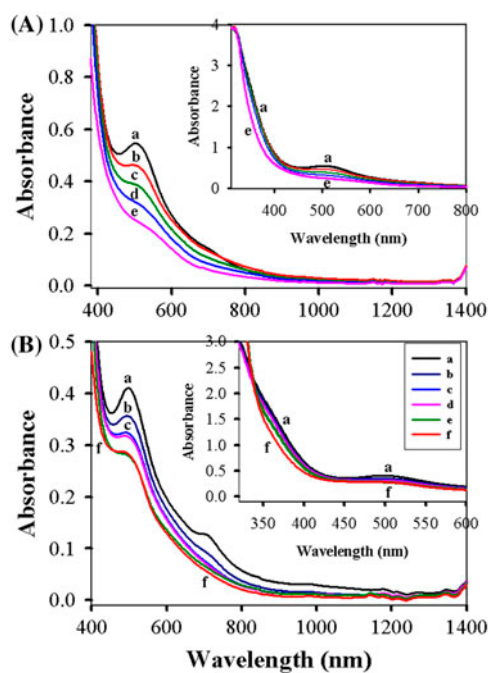


Figure 13. Panel A: (a) Electronic spectrum of **2a** (4.01×10^{-4} mol L $^{-1}$) in CH $_3$ CN in the presence of air. Then, twofold excess of solid PPh $_3$ was added and spectral change was recorded with time: (b) immediately after adding PPh $_3$, (c) after 30 min, (d) after 3 h, and (e) after 12 h from the time of adding PPh $_3$. Panel B: Electronic spectrum of **2** (3.16×10^{-4} mol L $^{-1}$) in DMF in the presence of air: (a) fresh solution, (b) after 25 h, (c) after 6 days, and (d) after 14 days. Then, excess of solid PPh $_3$ was added and spectral change was recorded with time: (e) 2 h after adding PPh $_3$, and (f) after 20 h from the time of adding PPh $_3$.

followed by dimerization as indicated from the presence of the 498 nm peak with reduced intensity, ultimately resulting in $[\{\text{Cr}^{\text{III}}(\text{L}^{\text{AP}})_2(\text{py})\}_2(\mu\text{-OH})](\text{OH})$ (**3**).

3.3.2. DMF solution in the presence of helium. We have already described in our previous report [10] the behavior of **1** in DMF in the presence of dry nitrogen using electronic spectral studies. It displayed a peak at 476 nm that started growing in intensity and reached a maximum intensity and then slowly started decreasing in intensity with time until it became steady within 3 h (figure S5, panel B of Supplementary Material). However, a more careful experiment revealed that after reaching a minimum, the intensity of all peaks started growing again then became steady (figure S5, panel C of Supplementary Material). This observation was very intriguing and prompted us to study the electronic spectral change of **1** in degassed DMF using helium that led to surprising results shown in figure 14. Initially, the intensity of the peak at 476 nm started increasing and reached maximum intensity within 11 min (figure 14, panel A), then started decreasing in intensity and reached a minimum, shown in figure 14, panel B, and then all the bands started growing again as observed in the case of nitrogen atmosphere. However, the overall intensity for all the peaks in helium atmosphere kept on increasing and became more than double the initial intensity with a blueshift of the

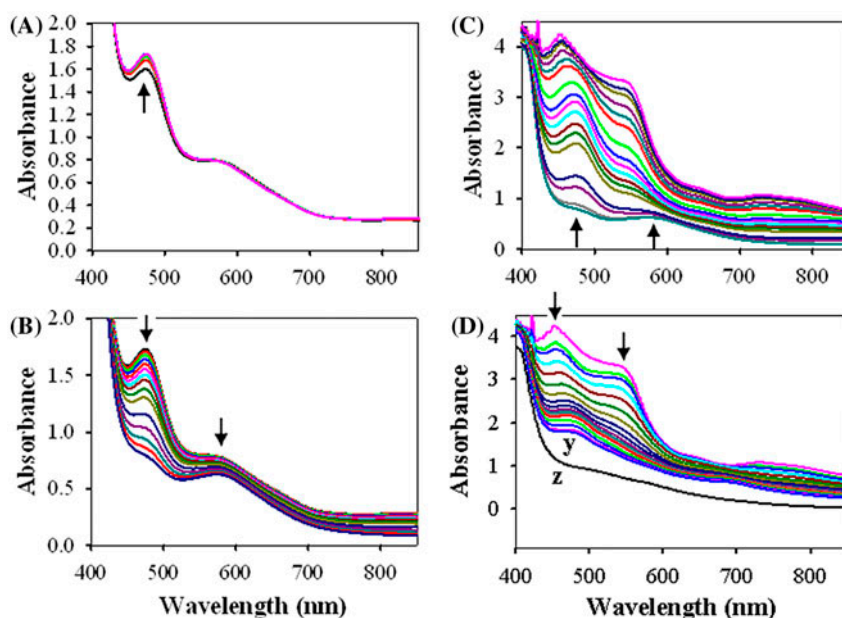


Figure 14. UV-vis spectral change of **1** (7.25×10^{-4} mol L⁻¹) in DMF in helium atmosphere at RT. Immediately after making the solution spectra were recorded with time: The intensity of the peak at 474 nm reaches maximum intensity within 7 min (panel A), then started decreasing in intensity and reached a minimum, shown in panel B, and then all the bands started growing again and the overall intensity was more than double the initial intensity with a blueshift of the charge transfer bands (panel C) and then the intensity after reaching a maximum started decreasing again (panel D). Total time taken for this entire process shown in these four panels is about 9 h when it reached a steady state (blue curve *y*). Then, it slowly decomposes with time when bottom black curve *z* in panel D was recorded after 24 h (see <http://dx.doi.org/10.1080/00958972.2015.1033412> for color version).

charge transfer bands (figure 14, panel C) and then after reaching a maximum intensity, the absorbance of all the peaks started decreasing again (figure 14, panel D) and became steady only after 24 h, ultimately resulting in a low absorbing species in the visible region (figure 14, bottom black curve in panel D).

It appears the overall process is very complicated and it is difficult to propose a mechanism for all the changes involved. The conversion of **1** to the square pyramidal deprotonated complex **B** was experimentally suggested from conductance and pH measurements [10] and now further supported by the proton NMR results. We have carried out theoretical studies to get an understanding of the species generated during the entire change in DMF in helium atmosphere. Ground state geometries of all the species (A–H) are optimized at the B3LYP/LANL2DZ level of theory (figure 15). First, let us start with the analysis of the experimentally verified conversion step of the initial complex **A** having a triplet ground state to the square pyramidal complex **B**. The DFT-optimized ground state of **B** has a triplet spin state with a deformed, asymmetrical structure. However, its lowest singlet state geometry (figure 15) has a highly symmetrical square pyramidal structure, situated roughly 0.9 eV above the triplet state. The theoretically predicted peak positions corresponding to singlet–singlet transitions at the ZINDO/CI and TDDFT levels were close to the experimentally observed peak position of this complex. We have considered that this is due to the presence of OH⁻ ligand

(which replaces H₂O in **A**) in **B** which is a potential π -donor. The $p\pi$ - $d\pi$ donation to the metal-based orbital is responsible for favoring the singlet spin state which gets populated. The observed peak is due to intense charge transfer of ligand-metal type [figure 16(a)], which is expected as ligands with lone pairs of relatively high energy (sulfur, selenium, *etc.*) are known for intense LMCT bands. This peak decreases after a certain period of time and then rises once again. The overlap of sulfur- and nitrogen-based orbitals with the metal can be seen from the figure of the HOMO [figure 16(a)] of complex **B**. The excited state LUMO [figure 16(a)] clearly shows an overlap of the metal orbital with a nitrogen-based orbital having an unpaired electron. Probably this

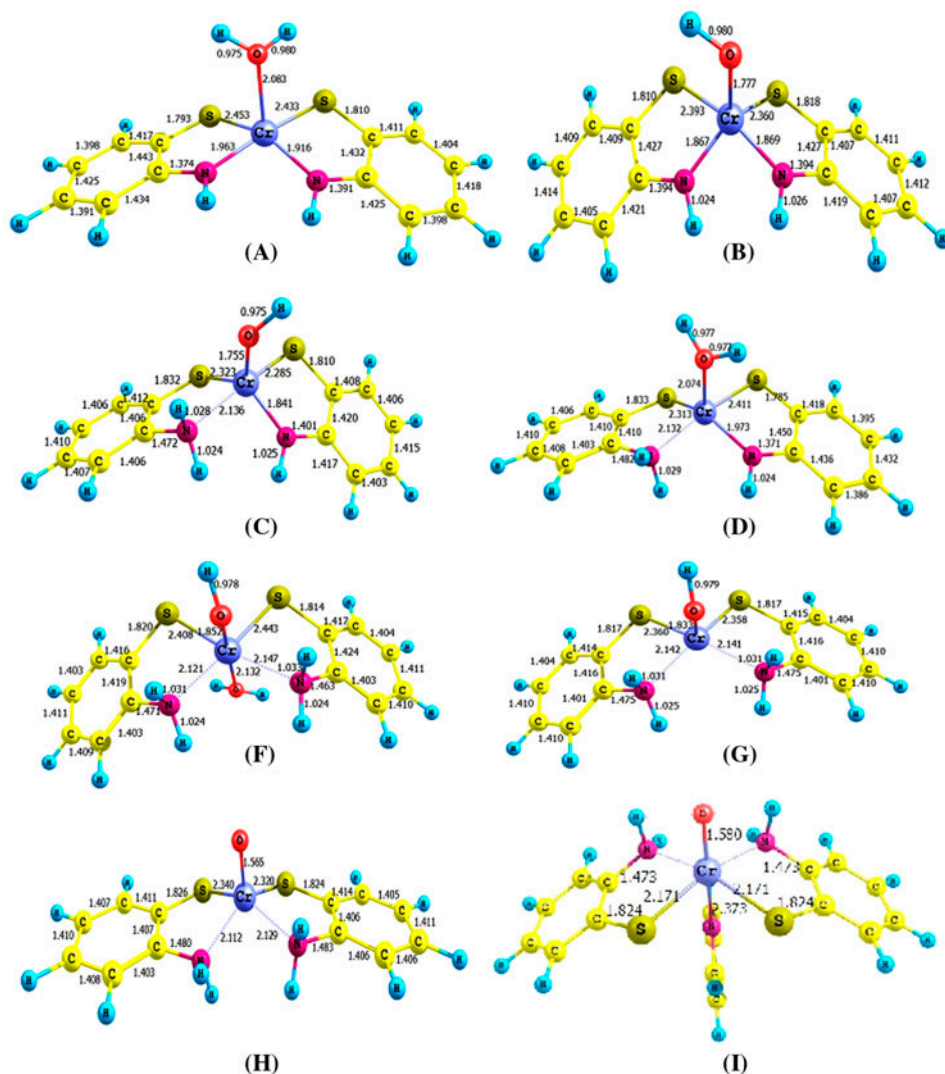


Figure 15. Ground state optimized geometries at the B3LYP/LANL2DZ level. The numbers indicate the distances between the respective atoms in Å.

overlap is not happening immediately after the vertical excitation, as no similar overlap is seen in the LUMO figure [figure 16(a)] at the ground state geometry, which means that the initial photo-excitation to the Franck–Condon excited state geometry is not involved in such metal–nitrogen overlap. It seems, at the relaxed excited state, a back donation to the nitrogen orbital from the electron-rich metal center takes place after the initial photo-excitation. This will certainly create a lone pair electron cloud on nitrogen and consequently a Cr(III) species may form with one of the two nitrogens; this will subsequently weaken the Cr–N overlap on that particular nitrogen. The singlet excited state species in this complex is expected to face a forbidden singlet–triplet transition which will increase the lifetime of this state and eventually it might get involved in a bimolecular process by attracting a proton from the medium to the lone pair on the nitrogen. As soon as this happens, there is an imbalance between the two ligand sides; one side now becomes reducing while the other is oxidizing. This five-coordinated Cr(III) complex (**C**) has been optimized at the B3LYP/LANL2DZ level and is found to be puckered (figure 15), as substantial Cr–N overlap is seen on one side, whereas no such overlap is on the other side. The predicted peak of this complex has lower absorbance than **B**. This charge transfer band is of ligand–metal (L–M) type and found to be primarily arising due to the HOMO–LUMO transition [table 1, figure 16(b)]; the HOMO–LUMO gap in **C** is lower (2.3 eV) than that of **B**. This predicted puckered complex (TBP-type) cannot accommodate another ligand at the sixth position to gain stability due to the lack of any possible accommodation space. Therefore, for better stability, it can be expected to attain a square pyramidal form; however, there exists no such ground state geometry for this complex as evidenced by the DFT results. If we replace OH^- by H_2O , the ground state geometry of the resulting complex (**D**) becomes symmetrical square pyramidal with triplet spin state, which is probably responsible for the intense charge transfer band at the lower wavelength side. The singlet state geometry of this complex is substantially higher energy in comparison with the triplet ground state. Presence of HOMO–1 \rightarrow LUMO+1 ($\Delta E_{\text{H}-1 \rightarrow \text{L}+1} = 2.59$ eV) and HOMO–1 \rightarrow LUMO ($\Delta E_{\text{H}-1 \rightarrow \text{L}} = 2.44$ eV) excitations have significant contributions in its absorption band. Intensity of a CT band depends on the extent of the transfer of charge from one end to the other. A closer look at the H–1 and L/L+1 in **D** clearly shows a complete transfer of electronic charge from left to the right side (donor to acceptor) and justifies the presence of this species (**D**) as the potential candidate for the unusually intense charge transfer band. This excitation is associated with a charge transfer of ligand–metal–ligand (LMLCT) [28a] type or ligand–ligand [28b,c] type with participation of the metal ion; the charge transfers in the earlier complexes are of ligand–metal (L–M) types. The nature of the double-peaked absorption maxima (figure 14, panel C) is quite similar to the peaks which usually arise from spin-orbit coupling [29] of two excited states with different spin multiplicities. It has been found that at the ground state (triplet) equilibrium geometry, a triplet excited state and the lowest singlet state have almost identical energies. These two states of different spin multiplicities are situated 2.01 eV above the ground state and may get involved (near 600 nm) in spin-orbit mixing which seems to be a reasonable explanation of the double-peak shaped maxima of the LMLCT band. However, ZINDO/CI studies on the singlet–singlet transitions have also predicted intense peaks for **D** at 465 and 497 nm (530 and 462 nm at TDDFT level). This intense peak decays slowly with time and the experimental results on the final product after completion of this change reaching a steady state after 9 h indicates the presence of only $-\text{NH}_2$ species rather than one $-\text{NH}$ and one $-\text{NH}_2$

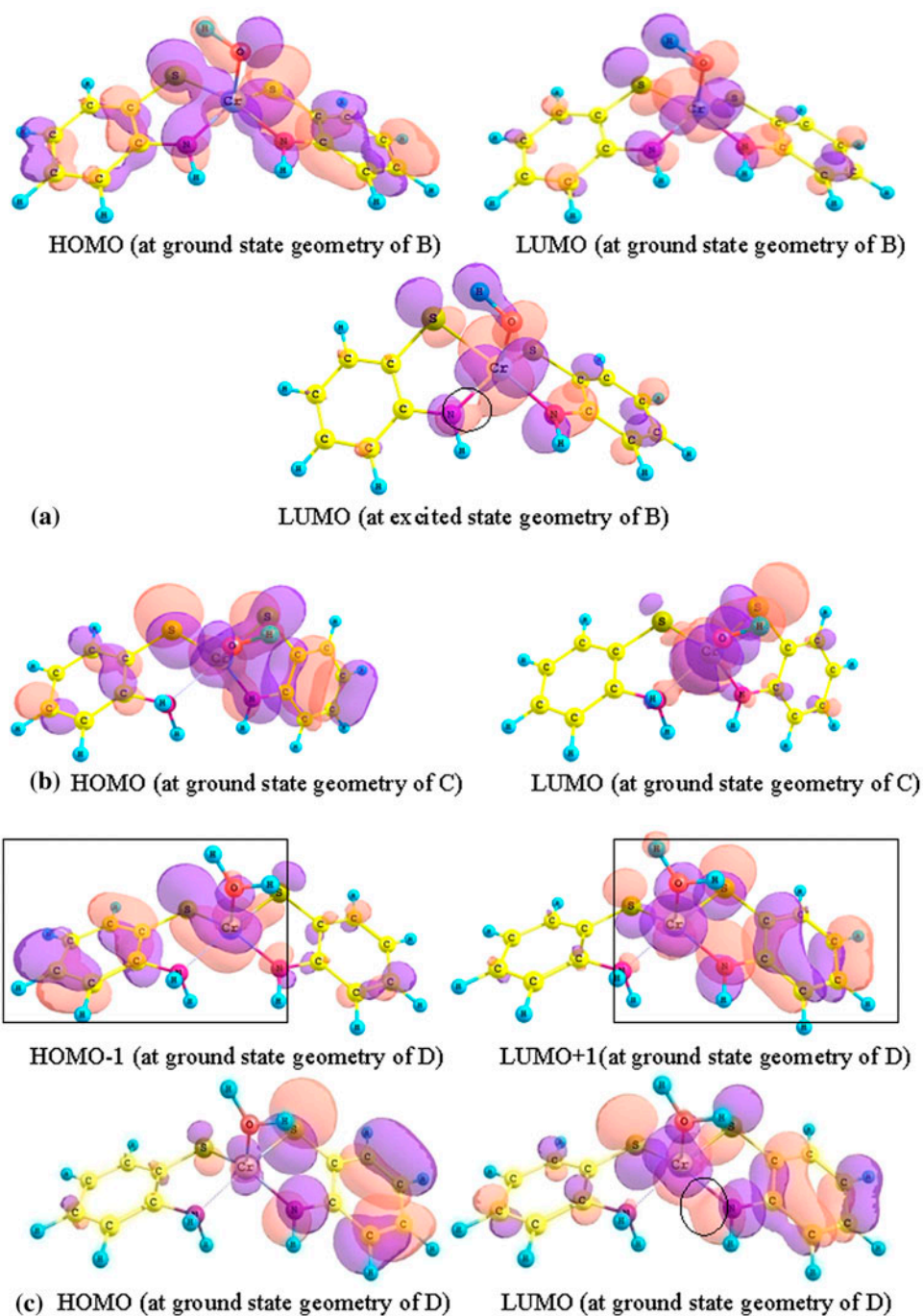


Figure 16. Important molecular orbitals responsible for charge transfer bands in (a) complex **B**, (b) complex **C**, and (c) complex **D**. The circle in (a) shows that filled metal and singly occupied nitrogen orbital overlap takes place in the LUMO of **B**. The portions marked with the box in (c) shows that the charge from the left hand side ligand portion of HOMO-1 is completely shifted to the other side of the ligand through the metal ion during the HOMO-1 – LUMO+1 transition in **D**. The circle in (c) shows that a filled metal and singly occupied nitrogen orbital overlap takes place in the LUMO of **D** which was not present in the HOMO.

Table 1. Predicted position of the peaks corresponding to singlet–singlet transitions, oscillator strength, and excitations involved in the respective transitions.

Complex	Level of calculation	Predicted peak positions (nm) of singlet–singlet transitions between 400 and 600 nm	Oscillator strength (f)	Dominating configurations of the respective transitions ^a
B	ZINDO/CI	479	0.18	H–1 → L+1(0.65), H → L+2(0.46), H → L(0.38)
		464	0.14	H–1 → L+2(0.85), H → L(0.21)
	TDDFT	452	0.13	H–3 → L(0.42), H–1 → L(0.32), H → L+2(0.30)
C	ZINDO/CI	584	0.14	H → L(0.74), H → L+2(0.43)
		445	0.12	H–1 → L(0.66), H–2 → L(0.60)
		425	0.12	H–2 → L(0.60), H → L(0.29)
D	ZINDO/CI	497	0.21	H–1 → L+1(0.68), H–2 → L(0.45), H → L+1(0.31)
		465	0.27	H–2 → L(0.54), H → L(0.40), H–1 → L+1(0.35)
	TDDFT	530	0.18	H → L+1(0.50), H → L(0.18), H–1 → L+1(0.16)
		462	0.04	H–5 → L(0.60)
		762	0.001	H–2 → L+1(0.50), H–1 → L+1(0.29)
H	TDDFT	481	0.001	H → L+1(0.63), H–1 → L+2(0.16)
		540	0.01	H → L+1(0.58), H–2 → L+5(0.27)
I (H with pyridine)	TDDFT	511	0.04	H–1 → L(0.52), H → L+1(0.28)

^aThe last column shows the contribution of the dominating configurations associated with the singlet–singlet transitions in the respective complexes, where H stands for HOMO and L stands for LUMO. As an example, H–1 → L+1(0.65) in complex **B** corresponding to the 479 nm peak in ZINDO/CI means that this particular singlet–singlet transition originates from the electronic excitation from HOMO–1 to LUMO+1 and its contribution is 0.65 (42%).

group, which indicates that the second –NH also gets protonated. According to our proposed scheme, this is possible if another electron from Cr(III) is donated to the ligand-based orbital having the remaining unpaired electron and becomes Cr(IV).

It must be noticed from figure 16(c) that filled metal and singly occupied nitrogen orbital overlap takes place in the LUMO of **D**. This indicates the formation of a lone pair orbital on nitrogen and thereafter protonation. Two possibilities (**F** and **G**) exist for a product of this process. None of these complexes have any peak between 300 and 700 nm at the ZINDO/CI level of calculation, which clearly suggests that the finally obtained species is not likely to be one of these two possibilities. The conversion of **D** to **F** can arise through an intermediate, denoted as **E**. It is well known that five-coordinate Cr(III) complexes are not very stable and it is probable that a H₂O gets attached to the sixth coordination site of **D**. Now, the conversion from **E** to **F** may happen due to electron donation of Cr(III) and subsequent proton transfer on nitrogen leaving one hydroxo ligand on Cr(IV). Conversion of **D** to **G** may also take place, which may again produce **F**, which is stable and the optimized geometry of **F** shows that this species is a highly symmetrical octahedral complex (figure 15). However, the possibility of this species as the stable final product is ruled out since it does not have any peak between 300 and 700 nm at the ZINDO/CI level of calculation and also the proton NMR spectrum that was recorded after the final change of **1** in d₆-DMSO in the absence of methanol did not display a peak around 2 ppm due to coordinated water, and also the broad peak that was initially observed at 10.32 ppm due to coordinated –OH was absent in the final spectrum recorded (figure S7 of the Supplementary Material), strongly suggesting that **F** is not the final product. There remains possibility of

another symmetrical neutral oxo species **H** as the final product which may arise from the deprotonation of -OH in **G**. Costentin *et al.* [11f] have demonstrated proton-coupled electron transfers using electrochemistry for $[\text{Os}^{\text{II}}(\text{bpy})_2\text{py}(\text{OH}_2)]^{2+}$ in water and have proposed the mechanisms of successive proton-coupled electron transfers for the conversion of the Os^{II} -aquo complex into the Os^{III} -hydroxo complex and finally into the Os^{IV} -oxo complex. Also, the mechanisms of proton-coupled electron transfers for oxidation of $\text{M}^{\text{II}}(\text{OH}_2)/\text{M}^{\text{III}}(\text{OH})/\text{M}^{\text{IV}}(\text{O})$ have been studied extensively with ruthenium complexes [11g–j]. Thus, the formation of an oxo-Cr(IV) complex **H** in the present case, owing to internal electron transfer and proton transfer, is not unlikely and this is most likely the case since the electronic spectrum recorded after 9 h (figure 14, bottom blue curve *y* in panel D) when it reached a steady state contains a band at 690 nm (absorbance ≈ 0.72) and another band at 478 nm (absorbance ≈ 1.8), very similar to those observed for **2** in the visible region strongly suggesting that **H** is the final product. This then slowly decomposes with time, resulting in a low absorbing species on standing in solution (figure 14, bottom black curve *z* in panel D). There are remarkable similarities in the electronic spectra of **H** with that of **2** except that the band positions are slightly red shifted (figure 10, curve *a*) in the latter compound due to coordination of pyridine *trans* to oxo as observed for other oxochromium(V) compounds [22c]. We have also done the calculation for pyridine coordinated **H**. The optimized geometry of this species **I** ($= \text{H} + \text{py}$) clearly shows the $\text{Cr}=\text{O}$ bond is slightly elongated upon pyridine coordination *trans* to the oxo group shown in figure 15. The HOMO–LUMO gap in **H** is 3.29 eV while that in **I** is 2.95 eV. This lower gap in the latter complex is due to the higher stabilization of its LUMO, caused by better charge delocalization on HOMO–LUMO excitation. During this electronic excitation from HOMO to LUMO, the electronic cloud shifts toward the pyridine and consequently the overall charge becomes distributed throughout the molecule (figure 17). This causes a red-shift of the absorption peak with respect to that of **H**. Attempt was also made to check for the possibility of formation of another species where DMF is coordinated to **H** in place of pyridine. The optimized structure of **H** + DMF complex has shown the inability of DMF to coordinate strongly with chromium ($r_{\text{Cr-DMF}} = 3.40 \text{ \AA}$); this is probably due to steric hindrance caused as the DMF approaches the metal ion. In contrast, the approach of pyridine which is planar is not sterically hindered (figure 15) and resulted in better metal-ligand binding ($r_{\text{Cr-N}} = 2.37 \text{ \AA}$). Also, it was found from the optimized geometry of all these species that the organic N–S donor ligands are *cis* in all cases (figure 15).

A possible scheme of the whole process for conversion of **A** to **H** is shown in figure 18. Overall, the intense charge transfer band can be attributed to a ligand–ligand charge transfer (LLCT) through the metal ion, and the responsible HOMO–1 \rightarrow LUMO/LUMO+1 excitations allow a complete transfer of charge from one end to the other. It is to be noted here that intermediate species containing ligands in two different oxidation states display strong intervalence charge transfer (IVCT) transitions [30], which disappear when both the ligands are reduced and protonated leading to the coordinated monoanion $(\text{L}^{\text{AP}})^{1-}$ in the final species (figure 14, blue curve *y* in panel D).

3.4. EPR results

A freshly prepared solution of **1** in pyridine in the presence of air displayed only a weak radical signal at $g \sim 2$ and the intensity of this line did not change with time. The frozen glass spectrum of this pyridine solution exhibited a broad line along with a sharp central line

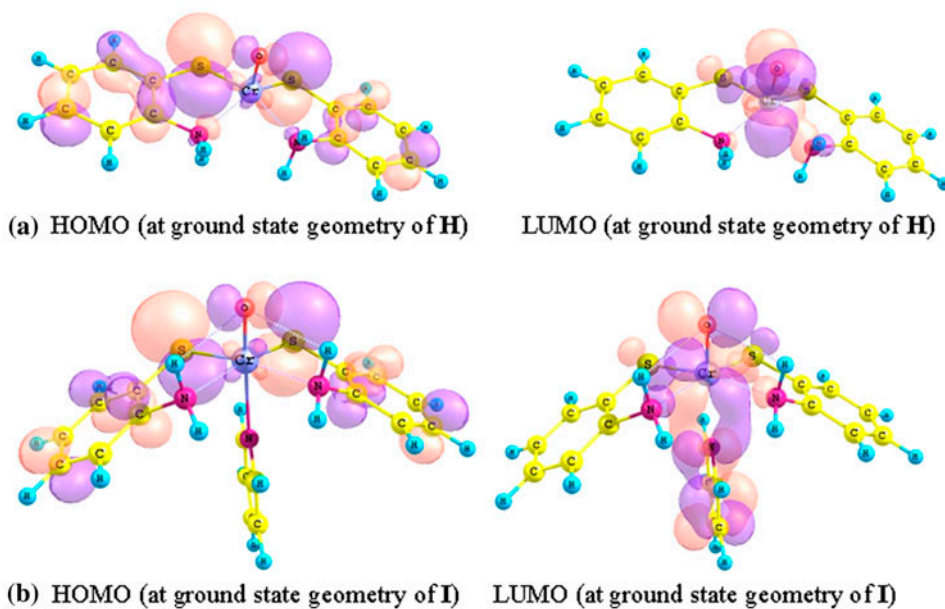


Figure 17. Important molecular orbitals responsible for charge transfer bands in (a) complex **H** and (b) complex **I**.

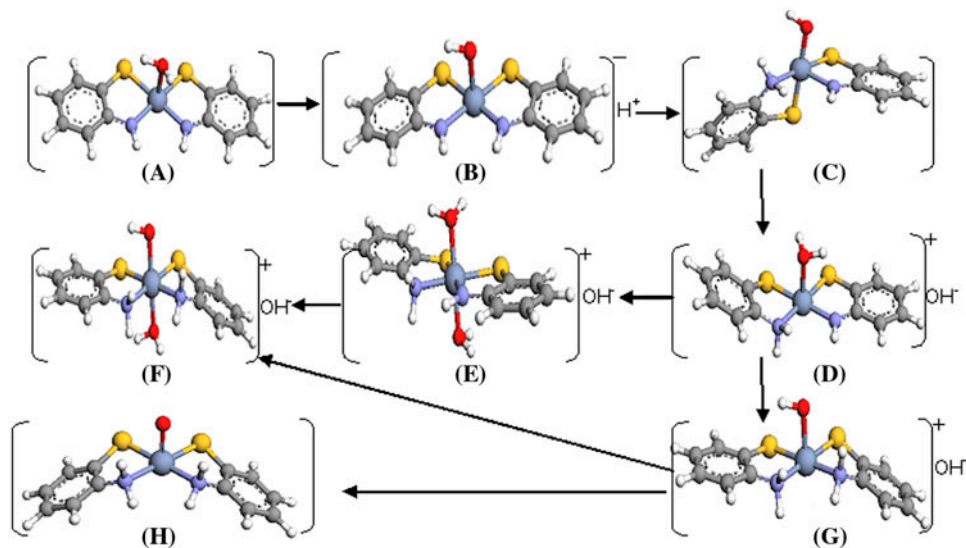


Figure 18. A possible scheme of the whole process.

($g = 2.05$), possibly originating from an intermediate metal complex containing radical ligand(s). However, **3** exhibits very strong and broad X-band EPR signals at both RT and LNT (figure 19). The powder EPR spectrum of **3** shows a peak-to-peak line width of ~ 410 G with $g = 1.98$ at RT. This line becomes even broader when the powder spectrum is recorded

at LNT, as evident from the peak-to-peak line width of 620 G with $g = 2.04$. This low temperature behavior of **3** is similar to that of **1**, suffering a contraction of lattice [20e, f].

Thus, the behavior of **1** in pyridine at RT is quite different from that observed [10] in its DMF solution in the presence of air, which is evident not only from the electronic spectral results but also from their EPR results. First, the pyridine solution of **1** did not exhibit the EPR spectrum of a d^1 Cr(V) species [31] as observed [10] in a freshly prepared DMF solution of **1** and only a weak radical spectrum was observed in pyridine solution during the entire process; the intensity of this line does not change with time. The DMF solution of **1** not only exhibited a monomeric Cr(V) EPR signal, its intensity initially increased and then started decreasing with time resulting ultimately in a weak radical signal at RT [10].

It strongly suggests that conversion of oxygen-bound species of **1** in pyridine to a final species does not proceed via formation of Cr(V) intermediate since it was not detected by EPR during the entire process. The aerial oxidation of the Cr(III) corrole complex, reported by Meier-Callahan *et al.* [32], to a Cr(V) species was inhibited by pyridine coordination. So the absence of any Cr(V) species in pyridine in the present case is not surprising. Thus, it appears that a Cr(IV) oxo species is generated in pyridine solution, otherwise rapid oxo transfer to PPh_3 for the formation of O=PPh_3 , mentioned above in figures 9 and 10, would not occur.

It is evident from the electronic spectral change of **1** in pyridine in the presence of air that it slowly binds to dioxygen forming a superoxo or hydroperoxy species as indicated from the strong charge transfer bands [33] in the NIR region (1249 and 853 nm), which in turn is converted to a O=Cr(IV) species **2**. The presence of an isosbestic point in the second phase of the electronic spectral change of **1** in pyridine [figure 9 (curves $j-w$ in panel B)] also indicates formation of the O=Cr(IV) species without the presence of any other intermediate. This is further supported by isolated **2** from the pyridine solution after 47 h. **2** undergoes slow but spontaneous change in pyridine forming an oxo-bridged Cr(IV)–Cr(IV) dimer (figure 12). The isolated product **2a** from this pyridine solution of **2** after 48 h is identical to that isolated from the pyridine solution of **1** after 96 h at RT. Both **2** and **2a** are converted to **3** on standing in DMF solution for several days. Compound **3** is consistent with the formulation of $[\{\text{Cr(L}^{\text{AP}})_2(\text{py})\}_2(\mu\text{-OH})](\text{OH})$ and inconsistent with the formulation of a $\mu\text{-oxo}[\text{Cr(L}^{\text{AP}})_2(\text{py})]_2$, as indicated from the following observations. It is to be noted here that the IR spectrum of reported dinuclear Cr(III) compounds with a linear oxygen bridge [22, 34] exhibit asymmetric and symmetric Cr–O–Cr bands in the $860\text{--}790\text{ cm}^{-1}$

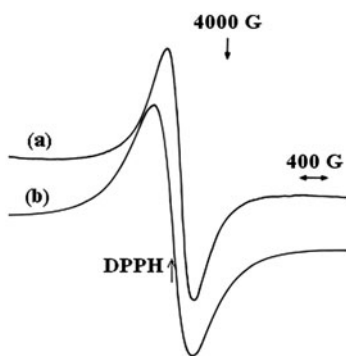
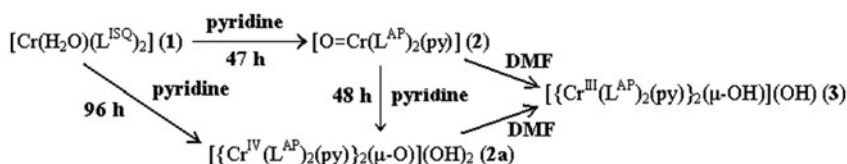


Figure 19. X-band EPR spectra of powder sample of **3**: (a) at RT and (b) at LNT.

region. Compound **3** does not exhibit any IR band in this region (figure S8 of Supplementary Material). IR spectrum of **3** clearly shows the presence of -NH_2 as well as pyridine. Apart from these, the far-IR spectrum of **3** shows a strong but broad band at 530 cm^{-1} (figure not shown), possibly arising due to overlapping of $\nu(\text{Cr-O})$ and $\nu(\text{Cr-N})$ with the out-of-plane ring deformation mode of pyridine because this mode at 405 cm^{-1} for free pyridine shifts to higher frequency on coordination [22a, 35]. The powder sample of **3** exhibits a strong and broad X-band EPR signal which is further broadened at LNT (figure 19). The DMF solution of this compound does not display an EPR signal at RT, but the frozen glass in DMF at LNT showed a strong and broad spectrum (figure not shown). The magnetic susceptibility measurement for this compound at RT (300 K) shows $\mu_{\text{eff}} \approx 5.1$ BM per dimeric unit, indicating the presence of weak antiferromagnetic interactions [20, 36, 37] between the metal ions in the solid state. Reported bimetallic Cr(III) compounds have $\mu_{\text{eff}} = 5.3$ BM per bimetallic unit at RT [37]. The measured magnetic moment for **3** is much higher than that reported for linear oxo-bridged dinuclear Cr(III) compounds possessing strong antiferromagnetic coupling between the Cr ions due to the presence of $d\pi(\text{Cr})\text{-}p\pi(\text{O})\text{-}d\pi(\text{Cr})$ orbital overlaps. For example, the μ_{eff} values for all salts of oxo-bridged Cr(III) dimer $[(\text{tmpa})(\text{SCN})\text{CrO}(\text{Cr}(\text{NCS})(\text{tmpa}))^{2+}]$ (tmpa = tris(2-pyridyl)methyl)amine) at 300 K were $0.8 \pm 0.1\ \mu_{\text{B}}$, corresponding to approximately 0.3 unpaired electrons per chromium. Also, no EPR signal could be detected for $[(\text{tmpa})(\text{SCN})\text{CrO}(\text{Cr}(\text{NCS})(\text{tmpa}))(\text{ClO}_4)_2 \cdot 0.5\text{H}_2\text{O}]$ at ambient and liquid-nitrogen temperatures [34c]. In contrast, **3** exhibits a strong EPR signal even at RT. Thus, taking this and $\mu_{\text{eff}} \approx 5.1$ BM into consideration and keeping in mind the tendency of **2**, the precursor of **3** to spontaneously dimerize in solution, it is suggested in the absence of a crystal structure that **3** is a OH-bridged dinuclear Cr(III) compound. The overall change for the conversion of **1** to **3** via **2** is presented in scheme 3.



Scheme 3. The overall changes for the conversion of **1** to **3** via **2**.

3.5. Electrochemical results

The electrochemical behavior of **2** has been studied in DMF containing $0.1\text{ M N}(n\text{-Bu})_4\text{PF}_6$ at a platinum working electrode using cyclic voltammetry (CV) in dinitrogen, and this whole experiment was completed within 5 min. For an initial negative scan between 0 and -1.50 V , there is a reduction peak near -0.90 V ; reversal of the scan gives a weak anodic peak at -0.69 V . For an initial positive scan between 0 and $+1.50\text{ V}$, there is an anodic peak at $+1.195\text{ V}$; reversal of this scan gives a reduction peak at $+1.037\text{ V}$ (figure 20).

Besides these cathodic and anodic peaks already mentioned, two successive weak oxidative responses are observed at -0.001 and $+0.604\text{ V}$, respectively, when the potential is scanned between -1.50 V and $+1.50\text{ V}$, and another broad reduction wave at -0.225 V . However, these two successive weak oxidative responses at -0.001 and $+0.604\text{ V}$ observed after an initial negative scan disappear in the second cycle. The reduction peak near -0.90 V is coupled to the weak anodic wave at -0.69 V , and the anodic peak at $+1.195\text{ V}$ is

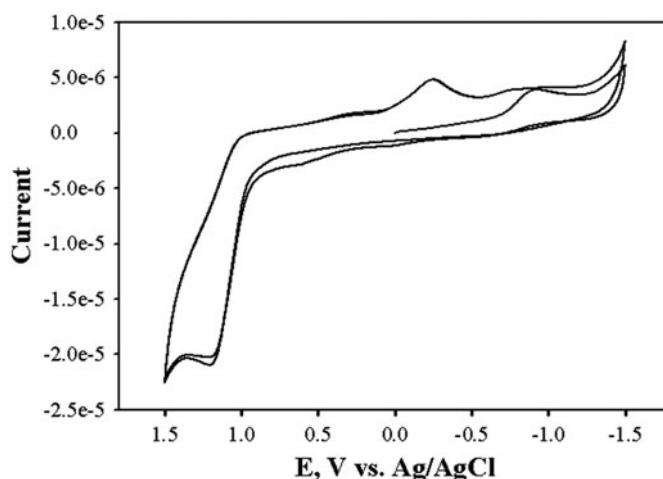
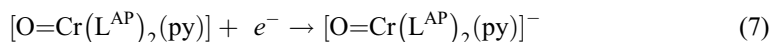
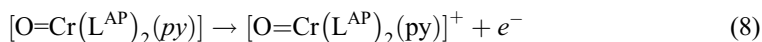


Figure 20. Cyclic voltammogram of **2** ($2.53 \times 10^{-3} \text{ mol L}^{-1}$) in DMF containing 0.1 M $N(n\text{-Bu})_4\text{PF}_6$ at a scan rate of 100 mV s^{-1} .

coupled to the reduction wave at + 1.037 V. The reduction peak at -0.225 V appears only after a positive scan and it is not observed if the potential is scanned only between 0 and -1.50 V , indicating that the species reduced at + 1.037 V is further reduced at -0.225 V . The reduction at -0.90 V is due to the process



while the oxidation wave at +1.195 V is due to



and this oxidized species $[\text{O}=\text{Cr}(\text{L}^{\text{AP}})_2(\text{py})]^+$ is reduced at + 1.037 V and is a quasi-reversible process ($\Delta E_p = 158 \text{ mV}$) indicating that the oxidized species is not stable. Recalling the noninnocent nature of the chelating ligands, it is difficult to assign the exact nature for the observed oxidations and reductions based only on this CV result.

4. Conclusion

Temperature-dependent magnetic studies on **1** from 20 to 300 K suggest a ferromagnetic coupling. Also, it is found that **1** undergoes spontaneous change only after deprotonation of the aqua ligand in solution prompting internal electron transfer followed by proton addition to the initially oxidized $-\text{NH}$ moieties leading to product(s) in which the coordinated chelating ligands are found to be in their reduced form *o*-aminothiophenolate(1 $-$) ($\text{L}^{\text{AP}1-}$) as revealed from the ^1H NMR results of **1** in d_6 -DMSO as well as from IR spectra of the isolated **2** and **3**, the products from pyridine and DMF, respectively. **2** is stable in solid but

undergoes dimerization on standing in pyridine or CH₃CN producing **2a**. **2** and **2a** have very similar electronic spectra and both of them are converted in DMF to the OH-bridged Cr(III) dimer **3**. Several attempts to grow single crystals for **2** and **3** were unsuccessful, so all the studies were confined to powder samples and solutions. Theoretical studies give a fairly good idea about the possible species involved in the spontaneous change of **1** in DMF in the absence of air. Optimized geometries of all these species suggest that the organic N–S donor ligands prefer to have a *cis* configuration in all cases.

Supplementary material

Figure S1: Electronic spectral change of **1** in DMSO in presence of air at RT. Figures S2–S4: Comparison of the ¹H NMR spectra of **1** recorded in d₆-DMSO (300 μL) containing methanol (200 μL) with time. Figure S5: Electronic spectral change of **1** in DMF in nitrogen atmosphere at RT. Figure S6: Plot of absorbance change at 1249 nm with time for the formation and for the disappearance of the species formed in the reaction of **1** with pyridine. Figure S7: Comparison of the ¹H NMR spectra of **1** recorded in d₆-DMSO in the absence of methanol with time: (a) within 1 h, (b) after 24 h. Figure S8: IR spectra of **1** and **3** in KBr.

Acknowledgements

M.K. thanks the Department of Inorganic Chemistry, Indian Association for the Cultivation of Science, Kolkata for help with the elemental analysis and IR spectrum. We thank the SAIF, IIT-Madras for NMR, EPR, and magnetic moment measurements, and the Central NMR facility at NCL, Pune for ¹H NMR studies with D₂O. A.P.K. thanks Dr C. Baby, SAIF, IIT-Madras and Dr C.S. Gopinath, Catalysis Division, NCL, Pune for help with the NMR studies; Mr Rangaraj Prasath and Dr P. Bhavana, Department of Chemistry, BITS-Pilani, K.K. Birla Goa Campus for help with the electrochemical studies and Ms. Nehal Bhatia for recording some of the electronic spectra. We also thank Drs G.V.R. Chandramouli and Balaji Sambandam for help in simulation. P.T.M. thanks the DST, Govt. of India, for a research Scheme (SR/S1/IC-53/2012) and also the INSA for its Senior Scientistship. We thank the Reviewers for their valuable suggestions to improve the manuscript.

Disclosure statement

No potential conflict of interest was reported by the authors.

References

- [1] S.I. Scott, A. Bakac, J.H. Espenson. *J. Am. Chem. Soc.*, **113**, 7787 (1991).
- [2] S.I. Scott, A. Bakac, J.H. Espenson. *J. Am. Chem. Soc.*, **114**, 4205 (1992).
- [3] (a) A. Hess, M.R. Hörz, L.M. Liable-Sands, D.C. Lindner, A.L. Rheingold, K.H. Theopold. *Angew. Chem. Int. Ed.*, **38**, 166 (1999); (b) K. Qin, C.D. Incarvito, A.L. Rheingold, K.H. Theopold. *Angew. Chem. Int. Ed.*, **41**, 2333 (2002).
- [4] K. Qin, C.D. Incarvito, A.L. Rheingold, K.H. Theopold. *J. Am. Chem. Soc.*, **124**, 14008 (2002).

- [5] J. Cho, J. Woo, W. Nam. *J. Am. Chem. Soc.*, **132**, 5958 (2010).
- [6] J. Cho, J. Woo, J.E. Eun Han, M. Kubo, T. Ogura, W. Nam. *Chem. Sci.*, **2**, 2057 (2011).
- [7] J.R. Budge, B.M.K. Gatehouse, M.C. Nesbit, B.O. West. *J. Chem. Soc., Chem. Commun.*, 370 (1981).
- [8] J.T. Groves, W.J. Kruper Jr, R.C. Haushalter, W.M. Butler. *Inorg. Chem.*, **21**, 1363 (1982).
- [9] K.H. Nill, F. Wasgestian, A. Pfeil. *Inorg. Chem.*, **18**, 564 (1979).
- [10] M.K. Koley, S.C. Sivasubramanian, S. Biswas, P.T. Manoharan, A.P. Koley. *J. Coord. Chem.*, **65**, 3329 (2012).
- [11] (a) E. Anxolabéhère-Mallart, C. Costentin, C. Policar, M. Robert, J.-M. Savéant, A.-L. Teillout. *Faraday Discuss.*, **148**, 83 (2011); (b) O.S. Wenger. *Acc. Chem. Res.*, **46**, 1517 (2013); (c) J.M. Mayer. *Ann. Rev. Phys. Chem.*, **55**, 363 (2004); (d) D.R. Weinberg, C.J. Gagliardi, J.F. Hull, C.F. Murphy, C.A. Kent, B.C. Westlake, A. Paul, D.H. Ess, D.G. McCafferty, T.J. Meyer. *Chem. Rev.*, **112**, 4016 (2012); (e) A. Migliore, N.F. Polizzi, M.J. Therien, D.N. Beratan. *Chem. Rev.*, **114**, 3381 (2014); (f) C. Costentin, M. Robert, J.-M. Saveant, A.-L. Teillout. *Proc. Natl. Acad. Sci.*, **106**, 11829 (2009); (g) S.J. Slattery, J.K. Blaho, J. Lehnes, K.A. Goldsby. *Coord. Chem. Rev.*, **174**, 391 (1998); (h) K.J. Takeuchi, M.S. Thompson, D.W. Pipes, T.J. Meyer. *Inorg. Chem.*, **23**, 1845 (1984); (i) R.A. Binstead, T.J. Meyer. *J. Am. Chem. Soc.*, **109**, 3287 (1987); (j) R.A. Binstead, B.A. Moyer, G.J. Samuels, T.J. Meyer. *J. Am. Chem. Soc.*, **103**, 2897 (1981).
- [12] R.R. Parr, R.G. Yang. *Density Functional Theory of Atoms and Molecules*, Oxford University Press, New York (1989).
- [13] C. Jamorski, M.E. Casida, D.R. Salahub. *J. Chem. Phys.*, **104**, 5134 (1996).
- [14] (a) R. Bauernschmitt, R. Ahlrichs. *Chem. Phys. Lett.*, **256**, 454 (1996); (b) R. Bauernschmitt, M. Häser, O. Treutler, R. Ahlrichs. *Chem. Phys. Lett.*, **264**, 573 (1997).
- [15] M.J. Frisch, G.W. Trucks, H.B. Schlegel, G.E. Scuseria, M.A. Robb, J.R. Cheeseman, G. Scalmani, V. Barone, B. Mennucci, G.A. Petersson, H. Nakatsuji, M. Caricato, X. Li, H.P. Hratchian, A.F. Izmaylov, J. Bloino, G. Zheng, J.L. Sonnenberg, M. Hada, M. Ehara, K. Toyota, R. Fukuda, J. Hasegawa, M. Ishida, T. Nakajima, Y. Honda, O. Kitao, H. Nakai, T. Vreven, J.J.A. Montgomery, J.E. Peralta, F. Ogliaro, M. Bearpark, J.J. Heyd, E. Brothers, K.N. Kudin, V.N. Staroverov, R. Kobayashi, J. Normand, K. Raghavachari, A. Rendell, J.C. Burant, S.S. Iyengar, J. Tomasi, M. Cossi, N. Rega, N.J. Millam, M. Klene, J.E. Knox, J.B. Cross, V. Bakken, C. Adamo, J. Jaramillo, R. Gomperts, R.E. Stratmann, O. Yazyev, A.J. Austin, R. Cammi, C. Pomelli, J.W. Ochterski, R.L. Martin, K. Morokuma, V.G. Zakrzewski, G.A. Voth, P. Salvador, J.J. Dannenberg, S. Dapprich, A.D. Daniels, O. Farkas, J.B. Foresman, J.V. Ortiz, J. Cioslowski, D.J. Fox, *Gaussian 09*. Gaussian, Inc., Wallingford, CT (2009).
- [16] A.D. Becke. *J. Chem. Phys.*, **98**, 5648 (1993).
- [17] C. Lee, W. Yang, R.G. Parr. *Phys. Rev. B*, **37**, 785 (1988).
- [18] M.A. Thompson, M.C. Zerner. *J. Am. Chem. Soc.*, **113**, 8210 (1991).
- [19] (a) D. Herebian, E. Bothe, E. Bill, T. Weyhermüller, K. Wieghardt. *J. Am. Chem. Soc.*, **123**, 10012 (2001); (b) H. Chun, T. Weyhermüller, E. Bill, K. Wieghardt. *Angew. Chem. Int. Ed.*, **40**, 2489 (2001); (c) P. Ghosh, E. Bill, T. Weyhermüller, K. Wieghardt. *J. Am. Chem. Soc.*, **125**, 3967 (2003).
- [20] (a) J.E. Huheey, E.A. Keiter, R.L. Keiter. *Inorganic Chemistry: Principles of Structure and Reactivity*, 4th Edn., pp. 459–468, Pearson Education (2003); (b) E.I. Solomon, M.A. Hanson, In *Inorganic Electronic Structure and Spectroscopy*, Vol II: Applications and Case Studies, E.I. Solomon, A.B.P. Lever (Eds.), pp. 25, 62, Wiley-Interscience, NJ (1999); (c) F.E. Mabbs, D. Collison. *Electron Paramagnetic Resonance of Transition Metal Compounds*, pp. 956–983, Elsevier, Amsterdam (1992); (d) G.V.R. Chandramouli, C. Balagopalakrishna, M.V. Rajasekharan, P.T. Manoharan. *Comput. Chem.*, **20**, 353 (1996); (e) S.K. Hoffman, D.K. Towle, W.E. Hatfield, P. Chaudhuri, K. Wieghardt. *Inorg. Chem.*, **24**, 1307 (1985); (f) N. Srihari, P.T. Manoharan. *Mol. Phys.*, **63**, 1077 (1988).
- [21] J. Vicente, A. Arcas. *Coord. Chem. Rev.*, **249**, 1135 (2005).
- [22] (a) K. Nakamoto, *Infrared and Raman Spectra of Inorganic and Coordination Compounds*, Part B, Applications in Coordination, Organometallic, and Bioinorganic Chemistry, 5th Edn., pp. 6, 23, 54, 55, 94, 172, Wiley, New York (1997); (b) E.G. Samsel, K. Srinivasan, J.K. Kochi. *J. Am. Chem. Soc.*, **107**, 7606 (1985); (c) K. Srinivasan, J.K. Kochi. *Inorg. Chem.*, **24**, 4671 (1985).
- [23] (a) E.S. Gould. *Coord. Chem. Rev.*, **135/136**, 651 (1994); (b) M.C. Ghosh, E. Gelerinter, E.S. Gould. *Inorg. Chem.*, **31**, 702 (1992).
- [24] M.K. Koley, S.C. Sivasubramanian, B. Varghese, P.T. Manoharan, A.P. Koley. *J. Coord. Chem.*, **65**, 3623 (2012).
- [25] S.E. Creager, R.W. Murray. *Inorg. Chem.*, **24**, 3824 (1985).
- [26] M.E. O'Reilly, T.J. Del Castillo, K.A. Abboud, A. Veige. *Dalton Trans.*, **41**, 2237 (2012).
- [27] M.E. O'Reilly, T.J. Del Castillo, J.M. Falkowski, V. Ramachandran, M. Pati, M.C. Correia, K.A. Abboud, N.S. Dalal, D.E. Richardson, A.S. Veige. *J. Am. Chem. Soc.*, **133**, 13661 (2011).
- [28] (a) J.S. Gancheff, F.E. Hahn. *Spectrochim. Acta, Part A*, **98**, 62 (2012); (b) A. Acosta, J.I. Zink. *J. Chem. Inorg. Chem.*, **39**, 427 (2000); (c) A. Kumar, Shih-Sheng Sun, A.J. Lees. In *Photophysics of Organometallics*, Chapter 1: Photophysics and Photochemistry of Organometallic Rhenium Diimine Complexes, A.J. Lees (Ed.), pp. 1–36, Springer-Verlag, Berlin Heidelberg (2010).

- [29] (a) C.J. Ballhausen. *Pure Appl. Chem.*, **44**, 13 (1975); (b) M. Triest, G. Bussière, H. Bélisle, C. Reber. *J. Chem. Educ.*, **77**, 670 (2000).
- [30] (a) R.R. Kapre, E. Bothe, T. Weyhermuller, S. DeBeer George, N. Muresan, K. Wieghardt. *Inorg. Chem.*, **46**, 7827 (2007); (b) R.R. Kapre, E. Bothe, T. Weyhermuller, S. DeBeer George, K. Wieghardt. *Inorg. Chem.*, **46**, 5642 (2007).
- [31] T.L. Siddall, N. Miyaura, J.C. Huffman, J.K. Kochi. *J. Chem. Soc., Chem. Commun.*, 1185 (1983).
- [32] A.E. Meier-Callahan, A.J. Di Bilio, L. Simkhovich, A. Mahammed, I. Goldberg, H.B. Gray, Z. Gross. *Inorg. Chem.*, **40**, 6788 (2001).
- [33] (a) A.B.P. Lever. *Inorganic Electronic Spectroscopy*, 2nd Edn, pp. 285–296, Elsevier, New York (1984); (b) A.B.P. Lever, E.S. Dodsworth, In *Inorganic Electronic Structure and Spectroscopy, Vol. II: Applications and Case Studies*, E.I. Solomon, A.B.P. Lever (Eds.), pp. 265–276. Wiley-Interscience, NJ (1999).
- [34] (a) M. Di Vaira, F. Mani. *Inorg. Chem.*, **23**, 409 (1984); (b) B.G. Gafford, R.A. Holwerda, H.J. Schugar, J.A. Potenza. *Inorg. Chem.*, **27**, 1126 (1988); (c) B.G. Gafford, C. O'Rear, J.H. Zhang, C.J. O'Connor, R.A. Holwerda. *Inorg. Chem.*, **28**, 1720 (1989).
- [35] B. Sopotranjanov, V. Stefov, M. Zugic, V.M. Petrushevski. *J. Mol. Struct.*, **482–483**, 109 (1999).
- [36] F.A. Cotton, G. Wilkinson, C.A. Murillo, M. Bochmann. *Advanced Inorganic Chemistry*, 6th Edn, pp. 744–746, Wiley, New York (1999).
- [37] R.K. Dean, S.L. Granville, L.N. Dawe, A. Decken, K.M. Hattenhauer, C.M. Kozak. *Dalton Trans.*, **39**, 548 (2010).